Open access • Journal Article • DOI:10.1029/2020TC006211

Exploring the Interactions Between Rift Propagation and Inherited Crustal Fabrics Through Experimental Modeling

Daniele Maestrelli, Domenico Montanari, Giacomo Corti, Chiara Del Ventisette ...+2 more authors

Institutions: University of Florence

Published on: 01 Dec 2020 - Tectonics (John Wiley & Sons, Ltd)

Topics: Rift

Maestrelli Daniele (Orcid ID: 0000-0002-3527-2394)

Montanari Domenico (Orcid ID: 0000-0003-1232-7230)

Corti Giacomo (Orcid ID: 0000-0001-7399-4438)

Del Ventisette Chiara (Orcid ID: 0000-0003-2429-7710)

Moratti Giovanna (Orcid ID: 0000-0003-3631-4733)

Bonini Marco (Orcid ID: 0000-0003-4818-8076)

Exploring the interactions between rift propagation and inherited crustal fabrics through experimental modelling

Daniele Maestrelli[1], Domenico Montanari[1], Giacomo Corti[1], Chiara Del Ventisette[2,1], Giovanna Moratti[1], Marco Bonini[1]

[1]CNR-IGG, Consiglio Nazionale delle Ricerche, Istituto di Geoscienze e Georisorse, Via G. La Pira, 4, 50121 Firenze, Italy.

[2]Dipartimento di Scienze della Terra, Università di Firenze, Via G. La Pira, 4, 50121 Firenze, Italy.

Corresponding authors: Daniele Maestrelli (daniele.maestrelli@gmail.com);

Marco Bonini (marco.bonini27@gmail.com)

Key points

- We perform analogue models to investigate the role of rift propagation vs inherited crustal fabrics.
- Inherited faults trending $\geq 45°$ to σ_3 are reactivated as transfer zones, while faults trending $< 45°$ act as accommodation zones.
- We compare models with four natural rifts, showing how inherited fabrics may control rift evolution.

This article has been accepted for publication and undergone full peer review but has not been through the copyediting, typesetting, pagination and proofreading process which may lead to differences between this version and the Version of Record. Please cite this article as doi: 10.1029/2020TC006211

Abstract

Continental rifting is a geodynamic process that involves the breakup of the crust, and may eventually evolve to sea floor spreading. Although it is often assumed to be a product of orthogonal divergence, continental rifting may result from oblique extension, and in several cases it is related to the rotation of plates or crustal blocks about a vertical axis. This implies the occurrence of rifts with straight but not parallel margins and rift axis-parallel gradients in extension velocity and amount of strain. The effects of rift propagation through the continental crust has only recently started to be addressed, and even less investigated is the interaction between rift propagation and inherited crustal fabrics. We have studied this issue by carrying out a series of analogue laboratory experiments. Modelling results suggest that inherited linear discontinuities in the model brittle upper crust that are oriented above a threshold angle (≥45°) from the orthogonal to the rift axis, have the ability to interact with rift-related structures. Depending on their orientation, such inherited discontinuities are reactivated as either transfer zones or rift-bounding faults. We compare our models with four natural prototypes in which rift propagation is likely to have occurred (the Trans Mexican Volcanic belt, the Gofa Province, the Gulf of Suez and the Kenya rift). For each case study, we show how the kinematics of propagating rifts is comparable to our model results, and we provide insights into how rift-related deformation may interact with inherited crustal fabrics.

Plain language summary

When the continental Earth's crust breaks due to tensional tectonic forces, deep depressions called continental rifts form. Over geological time, these features may ultimately evolve to oceans. This process is often assumed to occur symmetrically, but it has been shown that this is rarely the case. Indeed, continental rifting is often generated by the rotation of tectonic plates, which induces changes in the extension velocity along the length of the rift. In order to understand the evolution of many natural rifts, it is also important to determine how rifting interacts with existing discontinuities in the crust (e.g., faults). This issue has only been recently addressed by laboratory experimental models, in which natural processes are simulated at reduced time and length scales, using appropriate analogue materials to replicate the physical properties of natural rocks. We have performed a series of experiments that test this interaction, discovering that pre-existing faults can have a strong influence on the formation and evolution of continental rifts. To verify this correlation, we have compared our models with four (Mexico, Ethiopia, Egypt and Kenya) natural cases, finding that older faults have often influenced the rifting process and resulting structure.

1. Introduction

Rifting is one of the most important geodynamic processes that has shaped the Earth through crustal and lithospheric thinning, which may ultimately result in the break-up of continental plates. Whereas the process is commonly assumed to be cylindrical or symmetric in many rift settings, some examples show a rift axis-parallel gradient of deformation associated with rift propagation, which implies variations in extension rates along rift margins (Fig. 1a; e.g., Zwaan et al., 2020). These examples include the Red Sea, the Pacific Galapagos Rise, the Woodlark Basin in the SW Pacific Ocean, SE of Papua New Guinea, the South China Basin, and part of the Main Ethiopian Rift (Zwaan et al., 2020). Recent studies (e.g., Molnar et al., 2019; Zwaan & Schreurs, 2019; Zwaan et al., 2020) have shown how strain features in these settings can be

explained by the rotation of crustal blocks around an Euler pole, as a result of the so called "rotational tectonics" (e.g., Zwaan et al., 2020). Despite some pioneering attempts (e.g., Souriot & Brun, 1992; Benes & Scott, 1996; Mart & Dauteuil, 2000), the issue of rift propagation generated by rotation of crustal blocks has been addressed only recently in analogue modelling. In particular, Zwaan et al. (2020) showed that rotational rifting obtained by an expanding foam stretching an overlaying package of viscous and brittle material can properly reproduce a first order triangular or "V-shaped" rift propagation pattern, which shows similarity with the above mentioned natural cases worldwide. The seminal studies by Molnar et al (2017, 2018, 2019) reproduced lithospheric scale rift propagation induced by rotational tectonics, investigating how this process can influence and drive the formation of micro-continents (Molnar et al., 2018), and how propagating rifts may interact with weak zones in the lithospheric mantle and lower crust (Molnar et al., 2017, 2019, 2020). In fact, many rift systems (both with orthogonal extension and rotational propagation style) have been shown to interfere with inherited structures (e.g., Corti et al., 2007, Corti, 2012; Autin et al., 2013; Brune et al., 2017; Zwaan & Schreurs, 2017; Molnar et al., 2017, 2018, 2019; Rotevatn et al., 2018; Pongwapee et al., 2019). The relationships between the orientation of rift extension direction and that of lithospheric- and crustal-scale inherited structures is of primary interest, since inherited fabrics might affect rift genesis and evolution in multiple ways and at various scales (e.g., Corti et al., 2018).
In this study, we implement the approach of previous analogue modelling studies by presenting new laboratory experiments investigating the mutual effect between propagation of crustal extension and inherited fabrics. In particular, we focus on upper crustal brittle fabrics, whose influence on the deformation pattern resulting from rift propagation was not considered in previous experimental work. We apply our modelling results to the Trans-Mexican Volcanic Belt, Mexico, as well as to other propagating rifts worldwide, namely, the Gofa Province in Ethiopia, the Gulf of Suez, part of the Red Sea-Gulf of Aden system, and the Kenya Rift.

2. Analogue modelling procedure

2.1. Modelling strategy

Our experiments were designed by adopting a parametric approach, which consisted of the systematic variation of the orientation of brittle discontinuities (e.g., mimicking faults and fractures association, etc.). This modelling was carried out to evaluate if and how rift propagation may interact with crustal-scale inherited fabrics. The structure of the models was analysed quantitatively by means of photogrammetric digital elevation model construction, Digital Particle Image Velocimetry, and semi-automatic fault pattern quantification. This procedure provided the basis for comparing model results with the selected natural prototypes.

2.2. Model setup, materials and scaling

The conceptual model of rifting (Fig. 1a) was achieved through a modelling apparatus consisting of two moving plates (MP) fixed at their external tips and rotating around two pivot points. This model set-up allowed the progressive opening and consequent rift propagation within the overlying analogue brittle/ductile continental crust, whereby the minimum horizontal principal stress trends roughly orthogonal to rift propagation (Fig. 1b, c). The movement was obtained by dragging the plates with a stepper motor. A linear opening velocity of 10 mm/h was applied at the left hand side of each moving plate (see red dot in Fig. 1b, c). Due to the rotational movement of the MP, the velocity gradually decreased toward the pole of rotation along the propagating rift axis. The boundaries of the MP generated a velocity discontinuity (VD), whose effect was dissipated by employing a basal elastic rubber sheet (RS; green rectangle in Fig. 1b), the stretching of which allowed distribution of deformation and

avoided the formation of faults with unrealistic lengths and vertical throw. The RS is a natural latex elastic band 150 mm wide and 0.35 mm thick, that was attached to the MP for 10 mm on each side, using high-resistance double-side tape and then secured with American tape. The area of interest of each model corresponded to the centre of the RS, where boundary effects were minimized. The models reproduced a 2-layer, brittle-ductile continental crust (e.g., Bonini et al., 1997). We simulated the Upper Crust (UC) using a 1 cm-thick layer of a Quartz and K-feldspar sand mixture (80:20 proportion % in weight; see Montanari et al., 2017 and Del Ventisette et al., 2019) (Fig. 1c). The Lower Crust (LC) was simulated using a 1 cm-thick layer of Polydimethylsiloxane (PDMS) mixed with corundum powder in the proportion of 1:1 (% in weight) to obtain the correct density for the LC. All the details of material properties are reported in Table 1. The total thickness of the models (LC+UC) was 2 cm, over a total modelling area of about 70 x 35 cm and a more restricted area of interest of approximately 65 x 15 cm.

Models were scaled down to natural conditions in order to achieve correct length, dynamic, rheological and kinematic similarity (Hubbert, 1937; Ramberg, 1981; Weijermars & Schmeling, 1986). In particular, the geometrical scaling ratio was ~6.7 x 10^{-7}, such that 1 cm in the models simulated 15 km in nature. Scaling of stress, viscosity and velocity resulted in a natural extension rate of ~1 cm/yr. Details of the scaling ratios are reported in Table 1 and the detailed scaling procedure is reported in the Appendix A.

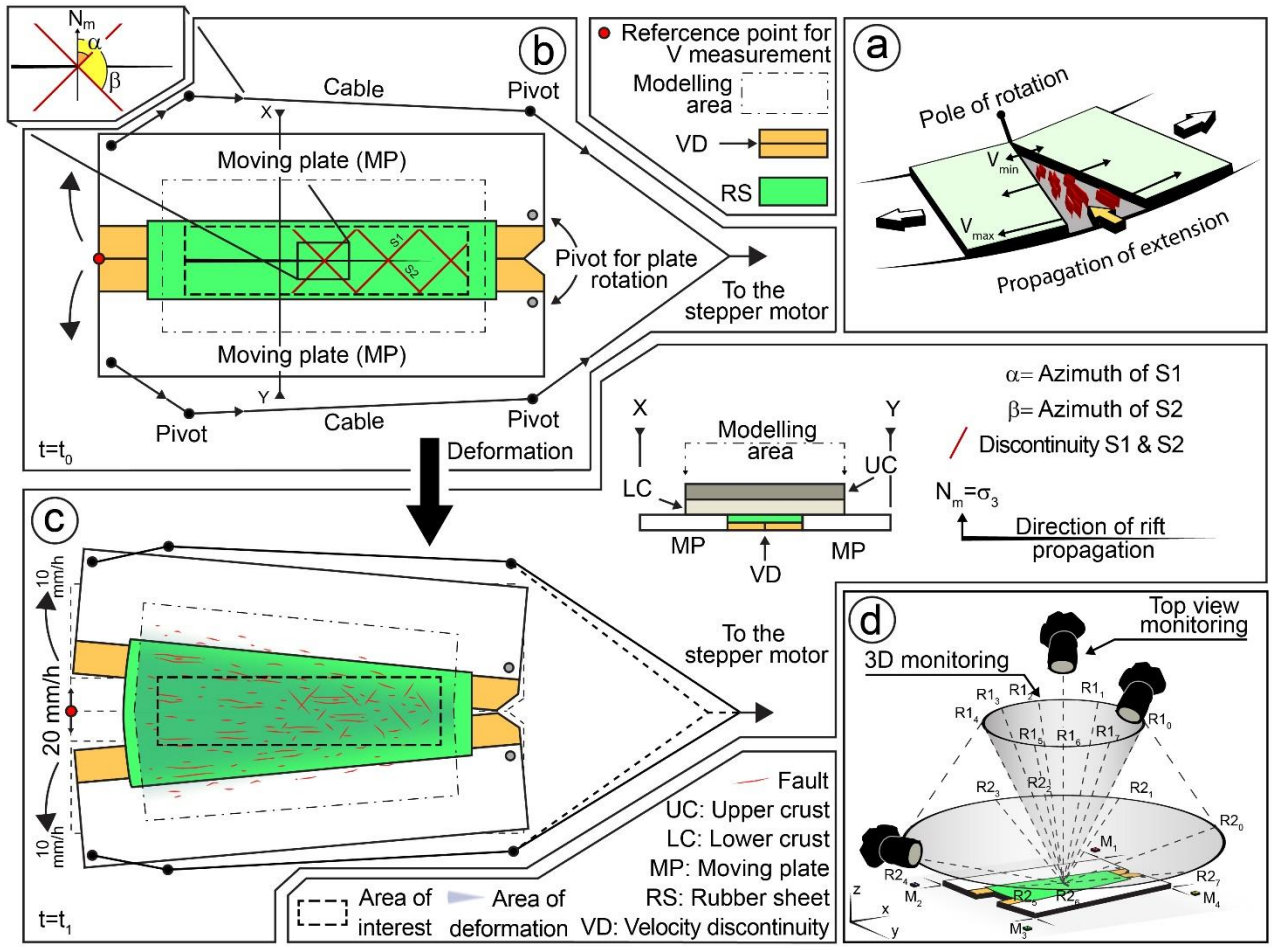

Figure 1. (a) Schematic sketch showing the conceptual rifting model produced by the movement of two crustal blocks pivoted to a pole of rotation, which leads to the propagation of extension (red planes mimic graben systems). **(b)** Schematic cartoon of the modelling apparatus. Two moving plates are rotated using a stepper-motor. Deformation was distributed using a basal rubber sheet (RS; green rectangle). Inherited structures (one or two

sets; S1 and S2) were reproduced within the brittle upper crust and placed at defined angles with respect to an arbitrary 'model North' (N_m) corresponding to the direction of σ_3, which is approximately taken as orthogonal to the direction of rift propagation (Table 2). **(c)** Top-view cartoon showing the rotational opening imposed to the model. **(d)** Sketch illustrating the adopted monitoring strategy: a fixed camera acquired high-resolution top-view photos, while a moving camera acquired high-resolution photos at pre-determined positions ($R1_0$-$R1_7$ and $R2_0$-$R2_7$) for elaborating photogrammetric digital elevation model (DEM) reconstructions. The correct scaling of DEMs was achieved through the use of locally geo-referenced markers (M_1-M_4).

Analogue material & parameter		Model	Nature	Model/Nature ratio
Qz-K-feldspar sand mixture (80:20 % in weight) (simulates the Upper Crust - UC)	Density ρ (kg m^{-3})	1440	~2700 (upper crust)	ρ *~0.53
	Internal friction coefficient μ	0.81-1	0.85	μ*~ 1
	Cohesion *c* (Pa)	~6	~$1x10^7$	c*=$6x10^{-7}$
	Thickness *h* (m)	0.01	15000	h*=$6.67x10^{-7}$
PDMS-Corundum (~ 1:1 % in weight) (simulates the Lower Crust - LU)	Density ρ (kg m^{-3})	1440	~2700	ρ*=0.53
	Viscosity η (Pa s)	$1.69x10^5$	10^{22}	η*=$1.69x10^{-17}$
	Thickness *h* (m)	0.01	15000	*h**=6.67 x 10^{-7}
Length *l* (m)		0.01	15000	l*=6.67 x 10^{-7}
Gravity *g* (m s^{-2})		9.81	9.81	g*=1
Stress σ' (Pa)				σ*=$3.53x10^{-7}$
Strain rate $\dot{\varepsilon}$ (s^{-1})		$5.55x10^{-4}$	2.66 $x10^{-14}$	ε*= σ*/η* = $2.1x10^{10}$
Velocity, *v* (m s^{-1})		$5.55x10^{-6}$ (0.08 m /$14.4x10^3$ s)	3.99 10^{-10} (=12.5 mm yr^{-1})	*v**= ε* l*=14000

Table 1. Characteristics of experimental materials and scaling ratios for the analogue models. The asterisk (*) denotes the ratio between model and nature for a given parameter. Characteristics of the granular material represented by the Qz-K-feldspar sand mixture are derived from Montanari et al. (2017) and Del Ventisette et al. (2019). The range for the internal friction coefficients is calculated considering the "peak friction" and "stable friction" values of the granular mixture.

2.3. Description of the experimental series

We present the results of 10 experiments (Table 2; raw data of these models are freely available to download from Maestrelli et al, 2020 at the link http://doi.org/10.5281/zenodo.3724666) out of 30 model runs for testing the relationships between rift propagation and inherited fabrics, as well as the reproducibility of results. To this aim, we introduced in the undeformed model one or two sets of discontinuities (referred to as S1 and S2) with specific azimuth angles (α and β, respectively) with respect to the orthogonal to the direction of rift propagation (Fig. 1b), which defines the arbitrary "north" in the experiments (N_m) and that approximately corresponds to the initial "instantaneous stretching direction" (ISD). The discontinuities are represented by sub-vertical artificial dilatation zones obtained by "cutting" the sand pack with a knife secured to adjustable guides. Reorientation of particles and variation of their original compaction causes local weakening of the sand mixture (e.g., Bellahsen & Daniel, 2005), which has the ability to focus deformation when the discontinuities are favourably oriented under the local stress field induced by model deformation. Discontinuities were introduced in the right half of the model with an average spacing of 4 cm (slightly varying depending on their orientation). In each model, we varied the orientation of discontinuities as reported in Table 2. Model RP-1 had no discontinuities and was used as "reference model". Models RP-2 and RP-3 tested only one set of discontinuities, in order to avoid possible mutual effects resulting from the presence of two sets. Models RP-4 to RP-9 tested the effect of rift propagation when two distinct sets of discontinuities trending at various angles are present in the experiments.

Model	**Azimuth of S1 (α) [°]**	**Azimuth of S2 (β) [°]**
RP-1	/	/
RP-2	30	/
RP-3	/	125
RP-4	30	125
RP-5	15	165
RP-6a	45	135
RP-6b	45	135
RP-7	60	120
RP-8	75	105
RP-9	90	180

Table 2. List of selected models discussed in this study. S1 and S2 represent the two sets of discontinuities introduced artificially in the layer simulating the upper crust, to simulate inherited crustal fabrics. Azimuth was measured in clockwise direction to the arbitrary "north of the model" (N_m), i.e., the orthogonal to rift propagation direction corresponding to the instantaneous stretching direction (ISD).

2.4. Monitoring and analysis of deformation

The evolution of model surfaces was constantly monitored through automatic acquisition of high-resolution top-view photos with 120 s time-steps. The finite topography was quantified using photogrammetric techniques (e.g., Donnadieu et al., 2003). Using structure from motion software (Agisoft Photoscan®), photographs taken from multiple perspectives of the model

surface were used to generate a 3D point cloud and from that a digital elevation model (DEM) (Fig.1d). The use of markers placed at fixed, and locally geo-referenced positions in the model system ensured that all calculated DEMs were at the same scale and in the same coordinate system (more details on this procedure are reported in Maestrelli et al., 2020). Quantitative analysis of models was performed using the free software FracPaQ (Healy et al., 2017) developed for MATLAB™, which allows the quantification of parameters that describe structural patterns in the models (e.g., fault trace length and orientation, Estimated structure Density -E_D- and Intensity, -E_I- Dilation Tendency of structures, etc.). Digital Particle Image Velocimetry (PIV) analyses were performed on selected model top-view photos to evaluate displacement vectors and quantify deformation using the free software PIVLab for MATLAB™ developed by Thielicke & Stamhuis (2014).

3. Results

3.1. Model RP-1: "reference model"

Model RP-1 was run without introducing discontinuities (Table 1) in order to obtain a reference model allowing observation of the basic system of rift development. From t=0 to t=80 minutes the opening of the MP caused incipient deformation within and outside of the area of interest, which is indicated by the darker area in Fig. 2. After t=80 up to t=120 minutes (Fig. 2a) small graben systems started to develop and link together, propagating toward the pole of rotation. Fault throw decreased from the proximal, left (western) hand side of the model (i.e., the area opposite to the pole of rotation), which underwent more finite and incremental deformation toward the eastern distal pole of rotation, where only shallow grabens were formed. Overall, the cumulative throw of graben systems led to a structural configuration similar to a "wide rift" setting (e.g., Buck, 1991). This deformation can be referred to a "deformation wedge" propagating toward the pole of rotation and increasing the number, length and vertical throw of the faults (Fig. 2a-f), which trend on average east-west (see Fig. 1b). These observations are supported by slope analysis performed on the DEM obtained for the final deformation stage (Fig. 3b)

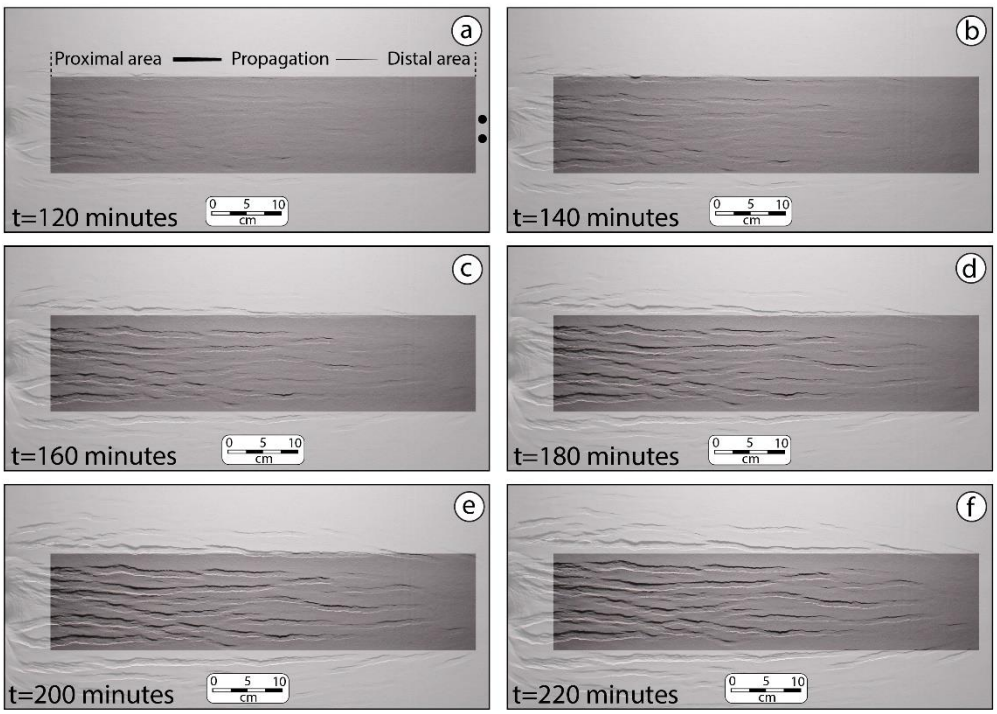

Figure 2. Top-view photos of the evolution of model RP-1. **(a)** Deformation began to be visible in the area of interest as a system of small-throw conjugate normal faults on the left hand side of the model, where the diverging velocity of the two mobile plates is higher. Black dots mark the MP pivot position. With increasing deformation **(b to e)** faults in the left hand side of the model gained larger displacement, developing well-structured graben systems, that propagated toward the distal part of the model (i.e. toward the pole of rotation). **(f)** After 220 minutes of deformation, the propagating rift reached the pole of rotation, where smaller grabens developed, while in the proximal part of the model the structures acquired larger vertical throws. Each step corresponds to ≈3.5 mm of deformation calculated at the left hand side of the model.

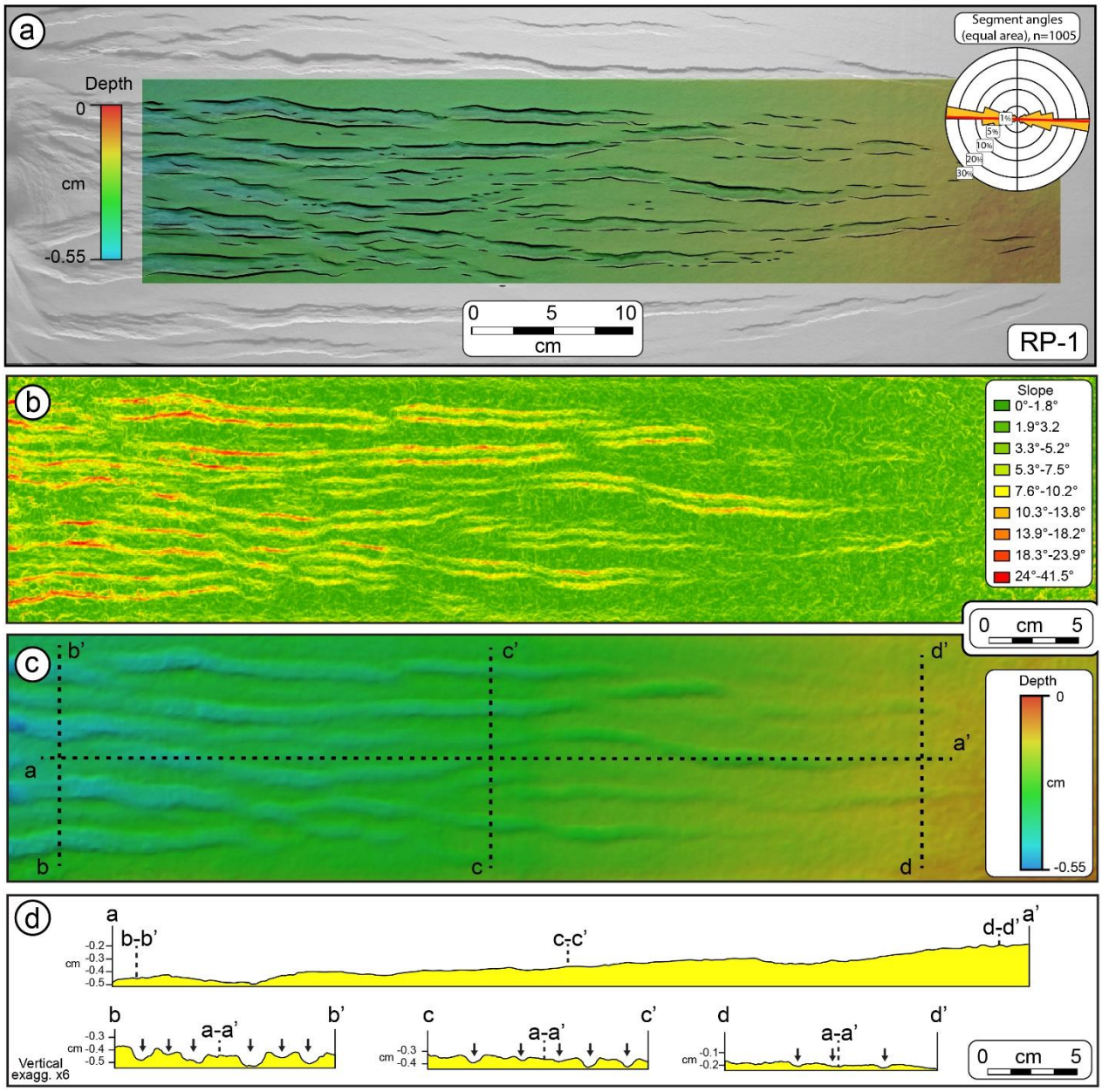

Figure 3. (a) Final stage of Model RP-1 with DEM and line drawing superimposed onto the area of interest. Rose diagram plot on the right-hand side, shows rift-related faults trend elaborated through FracPaQ; the red line marks the average fault trend. **(b)** Slope analysis of Model RP-1 DEM shown in **(c)**. Slope attribute highlights fault scarps, colouring DEM surface by angles of dip. Red colours highlight steepest scarps while green colours indicate flat surfaces. **(c)** DEM showing the trace of topographic profiles reported in **(d)**. **(d)** Topographic profiles (vertical exaggeration x6) along and across the area of interest, highlighting the presence and the morphology of grabens formed by rift propagation. Small black arrows mark the grabens considered for the parametric analysis shown in Figure 4.

Gradients in the degree of deformation were detected and highlighted by carrying out a slope analysis (Fig. 3b) of the model DEM (Fig. 3c) using ArcGIS® software, where slope attribute highlights fault scarps. Steeper fault scarps localize in the leftmost sector of the experiment, where the amount of extension is greatest and where fault density is highest. More to the right (i.e., closer to the pole of rotation), vertical fault throw is smaller (Fig. 3c), similar to the slope of the fault scarps. This is particularly evident by comparing topographic profiles obtained from the model DEM (Fig. 3d). Profile a-a' shows a gradual decrease of elevation from the distal area (i.e., close to the pole of rotation) toward the left hand side of the model, with a variation of surface elevation (Δd) of about 3 mm (see section a-a' in Fig. 3c). Grabens that formed in the proximal area of the model were the first to be created by MP rotation, and show a greater subsidence. Topographic profile b-b', orthogonal to the direction of rift propagation (Fig. 3c, d), shows the presence of six main grabens. Graben number progressively decreases in profile c-c' and d-d', as does graben width (w) and depth (d) (Fig. 4a). Fault density is higher in the left hand side and central portion of the model, while it is reduced close to the rotation pole. Areal quantification of this parameter is provided by maps of Estimated Density (E_D) and Intensity (E_I) of fault segments (Fig. 4b). Overall, these analyses indicate a V-shaped, rift-axis parallel intensity deformation gradient that progressively decreases toward the rotation pole.

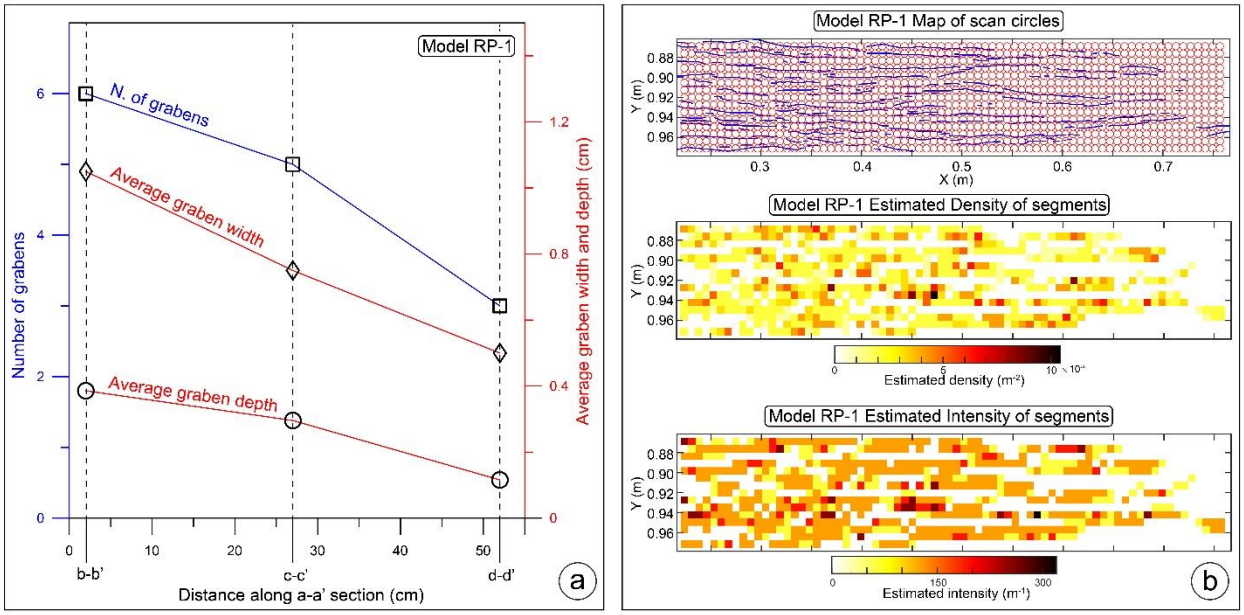

Figure 4. (a) Diagram comparing the parameters measured on the digital elevation model of Model RP-1. Grabens measured along three profiles are marked by black arrows in Figure 3d. The blue curve (with squares) shows a decreasing trend in the number of grabens along profiles b-b', c-c' and d-d' (Fig. 3c,d). The red curves show respectively the average graben width (diamonds) and depth (circles) measured along the same profiles. Both curves show a decreasing trend along the rift propagation axis. **(b)** Map of scan circles overlaying mapped faults (top panel) used for calculation of Estimated Density (E_D) and Intensity (E_I) (central and lower panels) of fault segments for Model RP-1. These parameters have been elaborated though the FracPaQ software (according to Mauldon et al.'s 2001 method). Radius of scan circles is 3.61×10^{-3} m (i.e., n. of scan circles along Y-axis is 15).

Finally, PIV analysis (Appendix B) performed on Model RP-1 (Fig. A2a,b) shows a gradient of velocity vector magnitudes that decrease toward the pole of rotation, with the velocities being effectively zero along the central axis of the experiment (Fig. A2a,b)

3.2. Models RP-2 to RP-9: "Inherited fabrics"

3.2.1. Models RP-2 to RP-4: inherited discontinuities trending N30° and N125°

Models RP-2 and RP-3 were designed to test the role of a single set of discontinuities, trending at angles of α=30° (set S1) and β=125° (set S2), respectively. Model RP-4 was then designed to test the two sets in combination (see Table 2).

In model RP-2 (set S1 with α=30°), the general development did not differ significantly from the evolution of model RP-1, showing incipient normal faulting in the proximal area of the model, which progressively propagated toward the rotation pole (right hand side of the model) to form a "V-shaped" subsiding wedge in the centre of the model. The wedge tip migrated progressively with the opening of the metal plates. Model deformation showed a clear gradient in terms of fault throw and fault number (both larger for faults on the proximal part of the model). The average fault trend (red line in Fig. 5a) is $N_m90°$. No evidence of reactivation of set S1 discontinuities was observed (Fig. 5a).

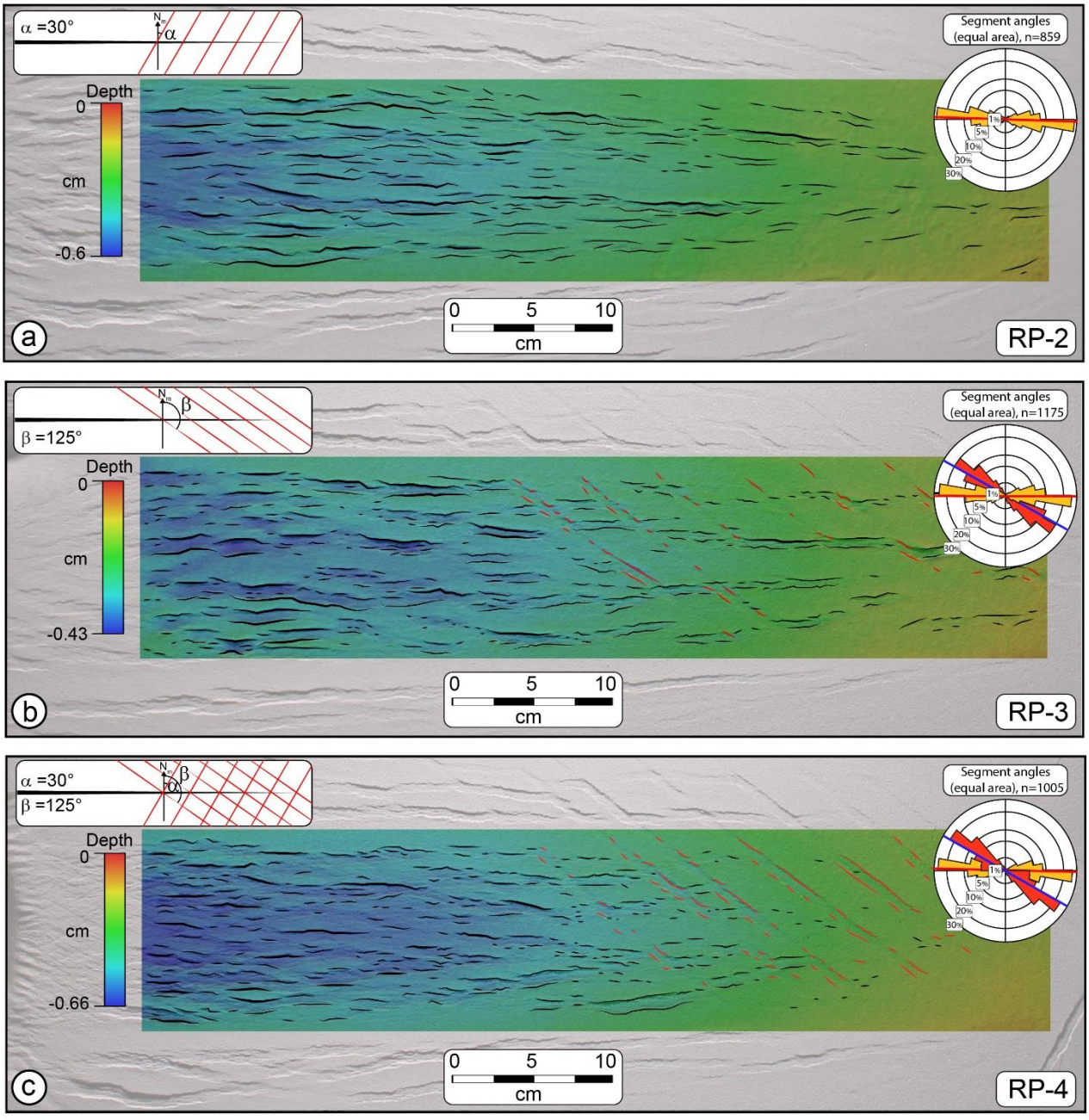

Figure 5. (a) Final top views of models RP-2, RP-3 and RP-4, with superimposed DEMs and line-drawing of structures in the area of interest. Red structures mark reactivated inherited discontinuities of sets S1 and S2 (see

sketches on the left-top corners). No reactivation of artificial discontinuities of set S1 (with α=N30°) can be identified on Model RP-2 **(a)** and RP-4 **(c)**, while inherited structures of set S2 (with β=125°) are clearly visible in Models RP-3 and RP-4 (**b** and **c**). Line stroke is proportional to fault throw. Rose diagrams show the relative trend of rift-related (orange) and reactivated (red) structures. Red and blue lines in the rose diagrams mark the average fault trend for rift-related and reactivated structures respectively.

Model RP-3 (Table 2; Fig. 5b) tested set S2 and showed a similar evolution to Models RP-1 and RP-2. Larger faults, with the largest vertical throw, reached a maximum length of ~9 cm (Fig. 5b), as in Model RP-2. Model RP-3 showed clear evidence for reactivation of the S2 discontinuities, which occurred in a scattered and discontinuous manner during deformation, in the form of incipient small graben systems trending $N_m125°$ (Fig. 5b).

Model RP-4 tested the presence of sets S1 and S2 together, and showed an overall evolution similar to models RP-2 and RP-3 (Fig. 5c). The average trend of structures ($N_m95°$) marks the prominent role of rift-related faults. As in Model RP-3, the S2 weak zones were reactivated (red lines in Fig. 5c, trending $N_m125°$), whereas the S1 discontinuities (with $\alpha = 30°$) were not reactivated, similarly to Model RP-2.
Notably, both in model RP-3 and RP-4, inherited structures to the left experience stronger reactivation than those to the right (closer to the distal area) and a more marked reactivation in the topmost area (in plan-view) than those in the bottom portion of the models.

3.2.2. Models RP-5 to RP-9: discontinuities with variable orientation

Models RP-5 to RP-9 tested the orientation of discontinuities trending at various angles with respect to the direction of rift propagation.

Model RP-5 (Fig. 6a) tested two sets of discontinuities with α=15° (set S1) and β=165° (set S2). In this model, the "V-shaped" propagation of the graben systems is extremely well developed. None of S1 and S2 sets was reactivated during model deformation. Despite no evident reactivation was visible (i.e. slip along inherited structures acquiring new throw), they may have subtle effects on the propagation of rift-related structures, since the latter are slightly segmented and shifted laterally from their straight propagation trajectory in correspondence of the inherited structures.
Model RP-6 tested the effect of discontinuities trending at lower angles (set S1 with α=45° and S2 with β=135°). This model was repeated three times, since it did not provide unequivocal indications on fault reactivation (we show here two out of all the performed attempts; Fig. 6b, c). In fact, two models out of three showed no reactivation of discontinuities set S1 and S2 (Fig. 6c shows one of the two models with no reactivation), while one model showed a slight reactivation of both sets (Fig. 6b), with no continuous faults and small amount of subsidence between grabens generated by reactivated fault couples. Nonetheless, as in Model RP-5, the discontinuities may not be reactivating but they seem to be exerting some control on the rift architecture.
Model RP-7 (Fig. 6d) tested discontinuity sets trending at α=60° (set S1) and α=120° (set S2). In the left hand side proximal area of the model, the cumulative deformation was accommodated by the development of $N_m90°$ trending (on average) graben systems. Both S1 and S2 weak zones were largely reactivated by rift-related deformation, causing the development of a "chessboard" pattern of reactivated structures.
Model RP-8 (Fig. 6e) showed complete reactivation of both discontinuity sets S1 (with α=75°) S2 (β=105°) developing rift-related structural patterns as well as a lozenge-shaped pattern accommodated by the reactivated weak zones.

Similarly, Model RP-9 showed a continuity of deformation proceeding from the rift-related structures in the area of incipient deformation (left hand side of the model in Fig. 6f) to the area of reactivation of S1 discontinuities (with α=90°). A "V-shaped" depression did not develop and strain was accommodated along the reactivated weak zones. In the area between two reactivated discontinuities (marked by red lines in Fig. 6f) we observed parallel rift-related structures. These latter show less variability in their orientation than those observed in the left hand part of the model (where no pre-existing discontinuities were cut), together with a longer continuity. Besides, no evidence of fault reactivation was observed for S2 discontinuities, which trend at high angle to the direction of rift propagation (β=180°).
Overall, the behaviour of the reactivated discontinuities (i.e., Models RP-6a, RP-7, RP-8 an RP-9) was similar. In particular, a pair of conjugate faults developed in weak zones. Therefore, when reactivated, a single sand cut invariably localised a couple of faults delimiting a graben rooted at the cuts' deep end.

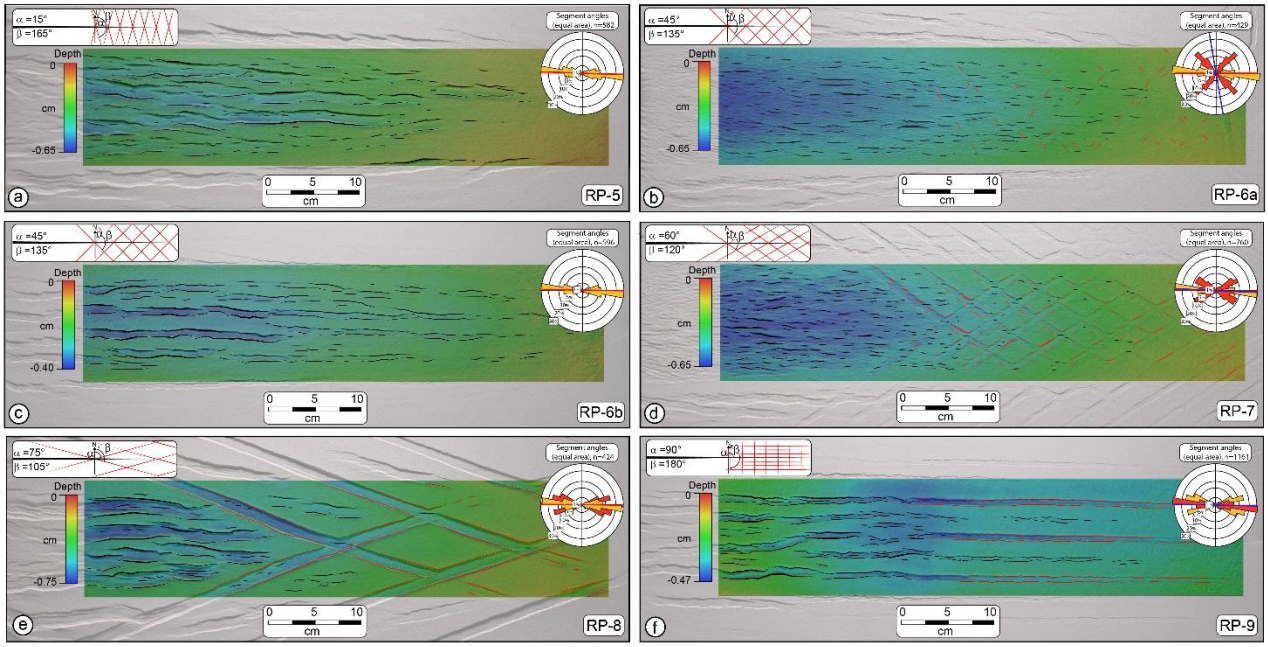

Figure 6. (a to f) Top-view photos of the final stage of Models RP-5 to RP-9 with different orientation of discontinuities with respect to the propagating rift (symbols as in Figure 6). **(b)** and **(c)** show two models testing the effect of inherited discontinuities trending at 45° (set S1) and 135° (set S2). In Model RP-6a **(b)**, discontinuities were only slightly reactivated, while in Model RP-6b **(c)** no reactivation of the two set was observed. Rose diagrams legend as in Figure 5.

4. Discussion

4.1 . Rift propagation vs inherited fabrics

Distribution and chronology of fault formation reflects the rotational nature of the model setup, implying a gradient of deformation propagating toward the pole of rotation. Fault displacement is also consistently higher for structures developed in the proximal regions of the models (where cumulative deformation is larger) and smaller in distal areas adjacent to the rotation pole, which experience lower strain. Velocity vectors appear orthogonal to the main graben faults (see PIV analysis in Appendix B), suggesting a dominant dip-slip component, while the reactivated structures can have a strike-slip component that is a function of their trend.

Overall, our reference Model RP-1 is in agreement with the modelling results shown by Zwaan et al. (2020) who reproduced the effect of rotational tectonics with a different, yet comparable model setup. A main difference occurs due to the presence of the rubber sheet, which we employed to distribute deformation, while Zwaan et al.'s (2020) models aimed to localize extensional faults at the centre of the model using a viscous "seed". Compared to their setup, the presence of inherited brittle discontinuities in our experimental series represents a further difference. Nonetheless, the role of inherited fabrics was also addressed by Molnar et al. (2017, 2018, 2019, 2020), who investigated rotational extension at a lithospheric-scale, highlighting the key role of crustal and lithospheric weak zones in controlling the formation of micro-continental blocks and testing their influence on surface deformation patterns. Despite a different aim and model setup, the overall surface deformation compares well with our models, as both show a "V-shaped" system of extensional faults with a clear decrease in the amount of extensional strain toward the rotation pole. Furthermore, Molnar et al. (2018) document how weak-zones are crucial to favour (or not) the detachment of micro-continents, highlighting that the orientation of inherited fabrics at lithospheric scale is a key factor controlling this process.
In our models, many ~N_m90° trending rift-related faults (i.e., the black lines in Fig. 6), were influenced by the reactivation of discontinuities. Discontinuity set S2 (with α=125°) has a noteworthy effect: these structures interacted with the rift-related faults during their propagation, deflecting the trajectory of the latter (Fig. 7a). Reactivated structures have often acted as transfer zones, exerting a hard linkage, forcing the propagation of rift-related faults to shift laterally (yellow arrows in Fig. 7a) and connecting the graben boundary faults. In addition, discontinuities trending at a low-angle to the direction of rift propagation were reactivated as highly dilatant structures, localising all of the extensional strain, as observed in model RP-8 (Fig. 6e).
Finally, there is a clear relationship between the trend of discontinuities and their reactivation: only favourably oriented discontinuities can be reactivated by extension (Fig. 7b). Specifically, in the experiments reported here, only discontinuities ranging between α=45° and β=135° are favourably oriented for reactivation. A further corollary is that the discontinuity angles tested in Model RP-6 (i.e., set S1 trending α=45° and set S2 trending β=135°; Fig. 5b,c) likely represent "limit angles" (LA) for reactivation, since out of the three experiments performed with this setup, two did not experience reactivation and the other one (i.e., Model RP-6a, Fig. 6b) showed only little evidence of reactivation. This behaviour is confirmed by the observation that no reactivation was observed for discontinuities oriented with an angle α<30° and β>135° (Fig. 7b). Nonetheless, as shown by model RP-5 and RP-6b, high-angle inherited structures that are not reactivated (i.e., that are not developing visible slip and generating throw) can also exert some control on the architecture of rift-related structures. In particular inherited structures can force rift–related faults to shift laterally from their propagation trajectory inducing some "soft linkage" (Fig. 7c), conversely to what is observed when inherited structures are fully reactivated (e.g., Fig. 7a). This contributes to an increase rift segmentation and shows that high-angle inherited structures (α< 45° and β>135°) may act as accommodation zones for rift propagation (Fig. 7b, c).

Further consideration can be given to the gradient of reactivation observed on inherited structures (e.g., Models RP-3, RP-4, RP-6a, RP-7; Fig. 5b, c and 6b, d). Both a proximal-distal gradient and an along-strike gradient of reactivation can be observed (e.g., Model RP-3; Fig. 8a). Both are controlled by the distance from the pole of rotation and by the trend of the inherited structures, respectively. These gradients are particularly evident if we extend the observation outside the area of interest of the models (Fig. 8a). The proximal-distal gradient directly depends on the distance of a certain structure from the pole of rotation: the greater the distance, the greater the degree of reactivation, in agreement with the gradient of deformation

imposed by the rotational nature of the model setup (Fig. 8b). The along-strike gradient is controlled by the trend of the inherited structures, since the lower the angle, the greater the degree of reactivation (Fig. 8b). A decrease in the discontinuity trend angle implies that the left hand side of a given inherited structure is closer to the proximal area, while its right portion is farther. This imply an increase in the along-strike gradient (i.e., the reactivation is stronger in its proximal portion than in its distal one; Fig. 8a,b). For example, the along-strike gradient is zero for inherited structures that are orthogonal to the direction of rift propagation, while it coincides with the proximal-distal gradient for structures trending $N_m90°$. These considerations do not apply to inherited structures trending <45° and >135 (i.e., above and below the limit angles, LA; Figs. 8b and 9c), since they were not reactivated. In these cases, inherited structures acted only as accommodation zones.

Phillips et al. (2019) showed how inherited structures trending 45° to 90° to the direction of extension affected the localization (and the orientation) of rift-related structures in the North Sea, while structures trending at high-angles do not influence the formation of new faults, although they can contribute to basin segmentation. This consideration is in line with our observations, indicating that high-angle discontinuities can interact with rift-related structures to generate accommodation zones. Furthermore, the observation that inherited structures strongly influence rift-related fault propagation is in agreement with other natural examples. For example, Phillips et al. (2016) and Schiffer et al. (2019) report that inherited basement structures had a major influence on the evolution of rifting in offshore Norway and in the North Atlantic, respectively. This influence on rift development has been observed in analogue experiments. Corti et al. (2007) demonstrated that inherited structures are able to induce oblique-slip kinematics on newly forming rift-related structures, explaining the Z-shaped structural pattern observed in some natural rifts. Finally, a similar influence was demonstrated in the analogue experiments of Bellhasen & Daniel (2005) and Bellhasen et al. (2006), which showed structural patterns similar to those observed in our models (c.f. Fig. 7 with Fig. 5 in Bellhasen & Daniel, 2006).

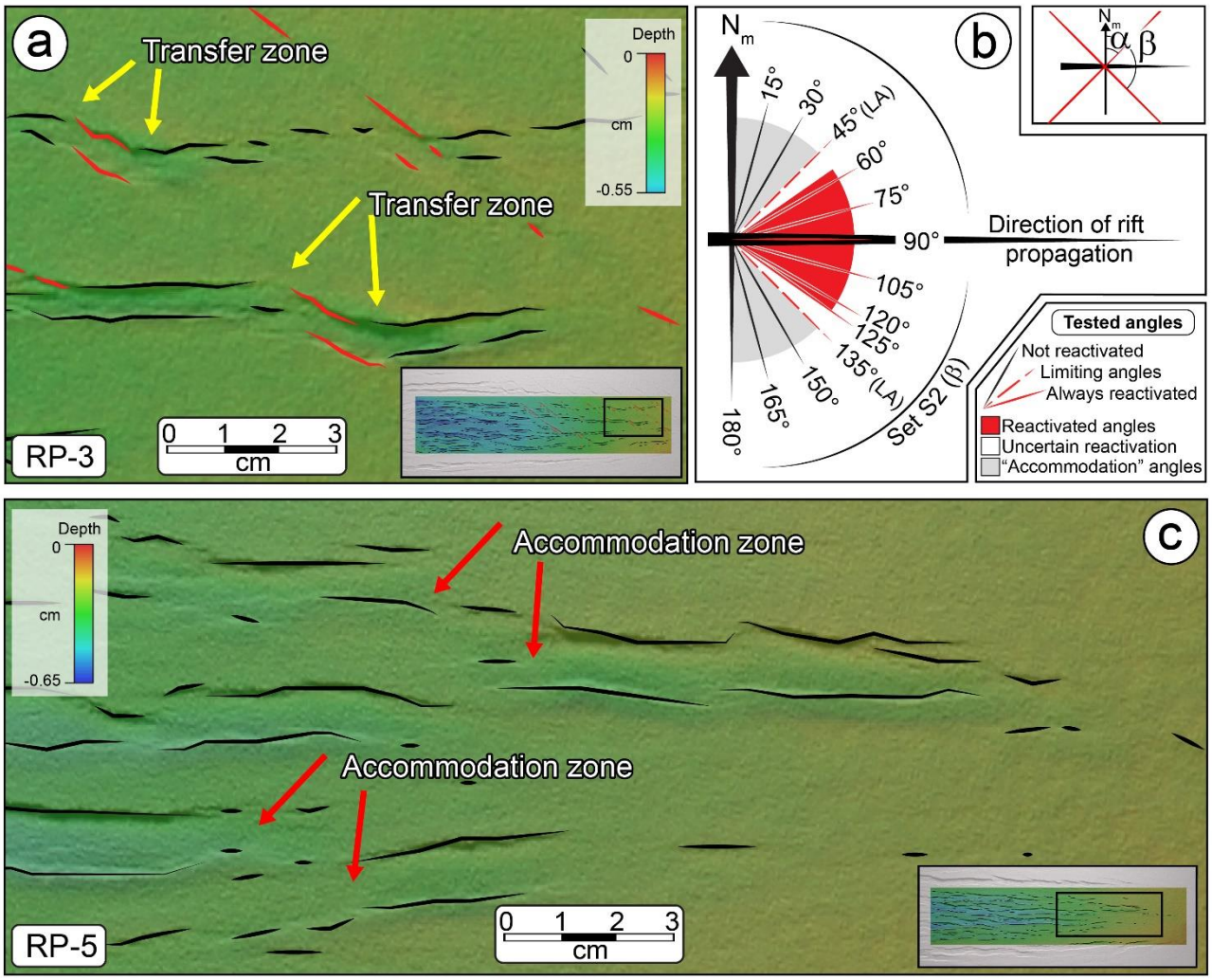

Figure 7. (a) Detail of Model RP-3 showing the reactivated inherited structures (red lines) acting as transfer faults (pointed by yellow arrows) for the rift-related structures (black lines). DEM overlays with transparency the top-view photo at a final stage of Model RP-3. **(b)** Sketch highlighting the reactivation field (red), the uncertain reactivation field (white) and the accommodation field (grey) obtained from the modelling (see also Table 2). LA: limit angle. **(c)** Detail of Model RP-5 showing the accommodation zones (pointed by red arrows) induced by high-angle inherited discontinuities, and the lateral shift of the propagating rift-related structures (black lines).

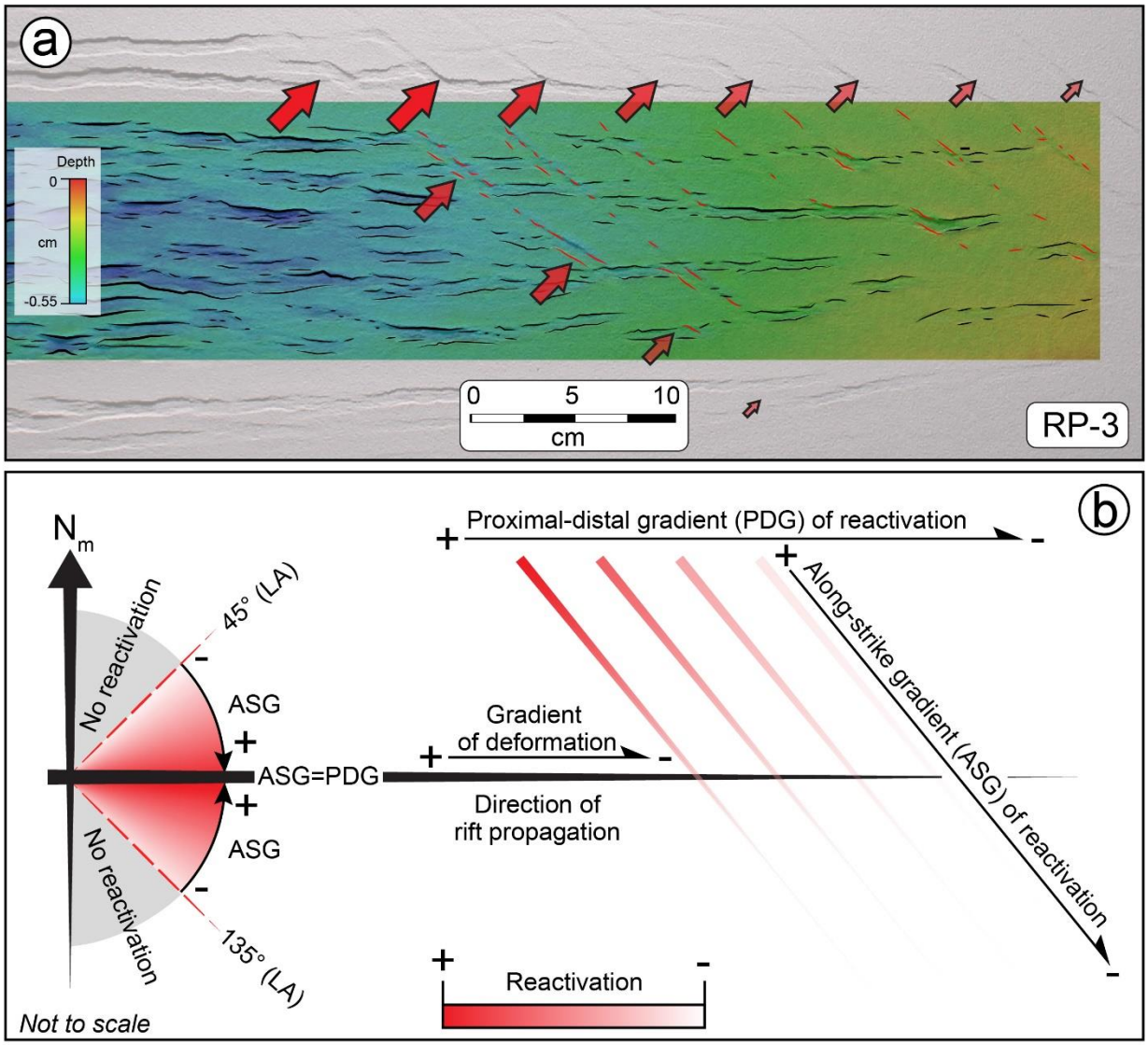

Figure 8. (a) Example of "reactivation gradient" observed in Model RP-3. The proximal-distal (PDG) and along-strike (ASG) gradients of reactivation are reported. They are controlled by the distance from the pole of rotation and by the trend of the inherited structures. Red arrows (with decreasing colour intensity) show the decrease in the degree of reactivation of inherited structures, highlighting the proximal-distal and the along-strike gradients. **(b)** Sketch illustrating the definition of proximal-distal and the along-strike gradients. LA: limit angle.

4.2. Comparison with natural cases

4.2.1. The Trans-Mexican Volcanic Belt

The motivation for the present study was to investigate both the role of tectonic inheritance and active tectonics in specific regions of the Trans-Mexican Volcanic Belt (TMVB), which is a large-scale, NW-SE trending, >1000 km long volcano-tectonic feature extending through central Mexico. Ferrari (2004) considered that continental rifting propagated southeastward as a result of progressive tearing of the Cocos slab. As a result of slab tearing and sinking, material from the asthenosphere was forced to migrate upward, inducing mafic magmatism, which was emplaced progressively from NW to SE in agreement with the direction of continental rift propagation (Fig. 9b). In the TMVB several inherited structures have been interpreted to interact with Miocene-Quaternary faults and to have localized eruptive centres (Garduño-

Monroy et al., 2009; Gómez-Vasconcelos et al., 2020). A variety of observation (e.g., focal mechanisms, borehole data, geological indicators) indicate a range of local extension directions throughout the TMVB (Heidbach et al., 2016). In central Mexico, Quaternary structures trending E-W and NNE-SSW suggests an average N-S Quaternary extension direction (e.g., García-Palomo et al., 2000; Fig. 9c). The large-scale crustal extension observed in our experiments has similar deformation gradients to those observed in the TMVB (Fig. 9a). Ferrari et al. (2012) showed how the crustal thickness doubles from WNW toward ESE, reaching a maximum value below Mexico City (Fig. 9b). A similar increase was also observed in our experiments, where the analogue crust thickens toward the pole of rotation (e.g., see section b-b' along model RP-1; Fig. 3d). Similarities were also observed when comparing extensional tectonic structures, which trend roughly parallel to the direction of rift propagation. Nonetheless, equivalents to ~N-S-trending structural systems (e.g., the Colima Rift and the Penajmillo Graben; Fig. 9b) were not observed in our experiments. These systems might be related to larger-scale N-S trending lithospheric inherited features (e.g. Ferrari et al., 2012), that were not simulated in our setup. Furthermore, fault density is higher in the area where crustal extension initiated, while less deformation is observed toward the SE, where no NW-SE trending structures are observed at surface. This is in agreement with the pattern of deformation reproduced by our models (compare with fault density and intensity analysis in Fig. 4b). Nevertheless, erupted surface deposits from recent volcanic centres obscured or covered evidence of tectonic structures. Volcanic centres show an older-to-younger trend toward the SE, suggesting that continental rifting propagated southeastward (Ferrari, 2004) (Fig. 9b). This kinematic model is in a good agreement with our analogue experiments. In the central area of the TMVB, the Morelia-Acambay Fault System (MAFS) shows important similarities with our model RP-4 (cf. Fig. 9c and Fig. 9d). Here, a system of roughly E-W-trending Miocene-Quaternary grabens, that are aligned with historical seismicity (Fig. 9c) are dissected by older (~30 Ma) NW-SE trending faults, which show evidence of right-lateral reactivation (Garduño-Monroy et al., 2009).

In order to compare our models with nature, we have rotated model RP-4 to fit the geographic north (N; see Fig. 9). The trend of faults in the MAFS is comparable to the S2 discontinuities in Model RP-4 (anisotropies trending β=125° corresponding to N140°in nature) and Models RP-6a,b (anisotropies trending β=135° in the model corresponding to N150°in nature).

Models RP-6a,b showed that discontinuities with β=135° are occasionally reactivated during extension, while discontinuities trending β=125° are always reactivated. This is in good agreement with the setting of the MAFS, which has been interpreted as a reactivated fault system (Garduño-Monroy et al., 2009). Model results suggest that fault reactivation can be related to the propagation of rift-related extensional faults. Furthermore, Model RP-4 (as well as Model RP-3) showed that inherited faults are often reactivated with a strike-slip component, which may offset the E-W trending rift segments (see Fig. 7a).

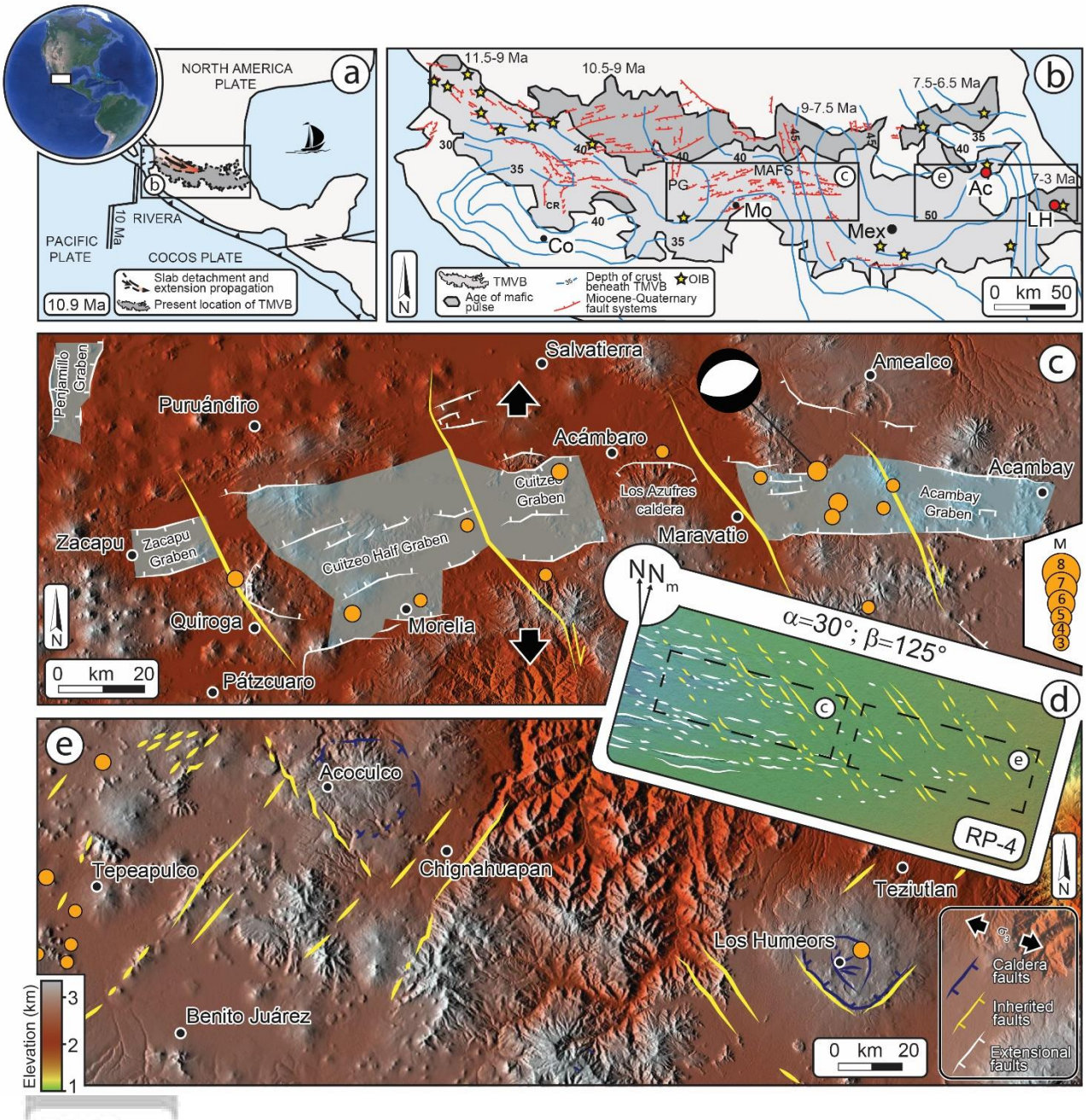

Figure 9. **(a)** Schematic map modified from Ferrari (2004) showing slab detachment and consequent propagation of extension (at 10.9 Ma) from NW to SE of the Rivera-Cocos subducting plates. **(b)** Present-day extension of the TMVB (light grey area) and propagation of mafic magmatic pulses (dark grey area) associated with slab detachment and consequent asthenosphere upwelling (modified form Ferrari et al., 2012; structures are simplified from Gómez-Tuena et al., 2007). Mo: Morelia; Mex: Mexico City; Co: Colima; PG: Penjamillo Graben; MAFS: Morelia-Acambay Fault System. Yellow dots indicate the location of Acocuclo and Los Humeros volcanic systems. **(c)** Satellite view of the MAFS showing inherited N150° trending faults (yellow lines). These structures have been reactivated and dissect Miocene-Quaternary extensional graben systems (faults from Garduño-Monroy et al., 2009). Direction of extension is taken from García-Palomo et al., 2000. **(d)** Model RP-4 rotated of 15° counter-clockwise with respect to N_m. Yellow lines indicate reactivated faults while white lines show rift-related structures. The results of Model RP-4 are consistent with the reactivation of MAFS faults. **(e)** Satellite view of the Acocuclo and Los Humeros area. The results of Model RP-4 suggest that only set S2 of inherited faults is favourably oriented for being reactivated by rift propagation. Faults are simplified from Avellán et al. (2019); García-Palomo et al. (2018) and Norini et al. (2019). Dashed black boxes in **(d)** indicate areas in Model RP-4 comparable to regions **(c)** and **(e)**. Orange dots in **(c)** and **(e)** show historical earthquakes (time interval 1900-2020). Seismicity and focal mechanisms of earthquakes with M≥3 are plotted from the USGS Earthquake Catalogue available at https://www.usgs.gov/natural-hazards/earthquake-hazards/earthquakes.

During progressive south-eastward propagation of crustal extension, the TMVB developed several large-scale volcanoes and calderas, some of which are the target of geothermal exploration.

Inherited crustal fabrics have been also reported in the easternmost sector of the TMVB, where they are represented by ~NE-SW and NW-SE-trending regional faults (Campos-Enriquez & Garduño-Monroy, 1987). The reactivation of inherited faults by continental rifting is an important issue, as these features have the ability to focus the ascent of magmas and related hydrothermal fluids. These structures may have played an important role in the localization of volcanic and caldera complex systems (e.g., the Acoculco caldera complex and the Los Humeros volcanic complex; Avellán et al., 2020; Fig. 9b). Here, magma and associated hydrothermal fluids might have migrated by exploiting secondary permeability associated with pre-existing structures. Specifically, two trends of discontinuities striking on average N45° and N140° are observed at Acoculco and Los Humeros (Campos-Enriquez & Garduño-Monroy, 1987; Carrasco-Núñez et al., 2017; Avellán et al., 2019; García-Palomo et al., 2018).

By rotating Model RP-4 15° counter-clockwise, we obtain α=30° and β=135° for discontinuities S1 and S2, respectively. This model showed that discontinuity set S2 was reactivated by crustal extension induced by the rift propagation, implying that the discontinuities trending around N140° in this area might have been reactivated. This result accords well with the observation that the NW-SE trending faults in the Acoculco caldera system show the highest alteration produced by circulation of hydrothermal fluids (Liotta & WP4 Working Group, 2019). A further observation based on our modelling results is that the interaction between rift-related faults and inherited fabrics may provide an efficient process for producing intersecting active structures, which provide favourable conditions for localising volcanic centres. This is confirmed by fault Dilation Tendency (T_D; Ferril et al., 1999) analysis (see Appendix C) on inherited faults performed on our models, showing that these structures are prone to be reactivated by the imposed stress field.

4.2.2. Gofa Province

A further case of comparison for our models is the Gofa Province (Moore & Davidson, 1978), north of the Chew Bahir basin and west of the southern segment of the Main Ethiopian Rift (Fig. 10). Here, a system of normal faults trending roughly SW-NE has been hypothesized to result from the rift propagation that resulted from local block rotation induced by the Somalian plate motion (Philippon et al., 2014). Furthermore, the role of NW-SE trending inherited structures in the basement has been invoked to explain the zig-zag deformation pattern acquired by the basins (Corti, 2009; Philippon et al., 2014). The rift-related structures (white lines in Fig. 10) are offset by inherited faults (yellow lines), documenting that the southern portion of the rifted area is wider than the northern sector, as often occurs in propagating rift settings. The inherited faults trend on average 45°-50° to the regional extension direction, with an instantaneous stretching direction (ISD) trending N105°(black arrows in Fig. 10; Philippon et al., 2014), which is similar to present-day GPS vectors that indicate an extension direction trending N100° (green arrows in Fig. 10; Kogan et al, 2012). Seismicity in the area is localized along both rift-related and inherited structures and the few available focal mechanisms show dip-slip to transtensional solutions. Assuming an orthogonal ISD to the direction of rift propagation (and coincident with N_m), the trend of reactivated structures is comparable with the trends tested in Models RP-6 and RP-7. As discussed above (Fig. 7), Models RP-6 suggest that 45° is a limiting angle for reactivation, and Model RP-7 indicates that discontinuities trending 60° to the ISD are always reactivated. This observation therefore supports the idea that inherited structures trending 45-50° to the ISD could have been reactivated during rift

propagation, influencing the development of the structural pattern of rift-related faults in the Gofa Province. In particular, Philippon et al. (2014) suggest that the NW-SE-trending structures could have acted as transfer zones, a conclusion confirmed both by seismicity and by our modelling. The presence of transfer zones is documented not only in Models RP-6a and RP-7 (Figs. 6 and 10) but also in many other models experiencing reactivation (see Fig. 7).

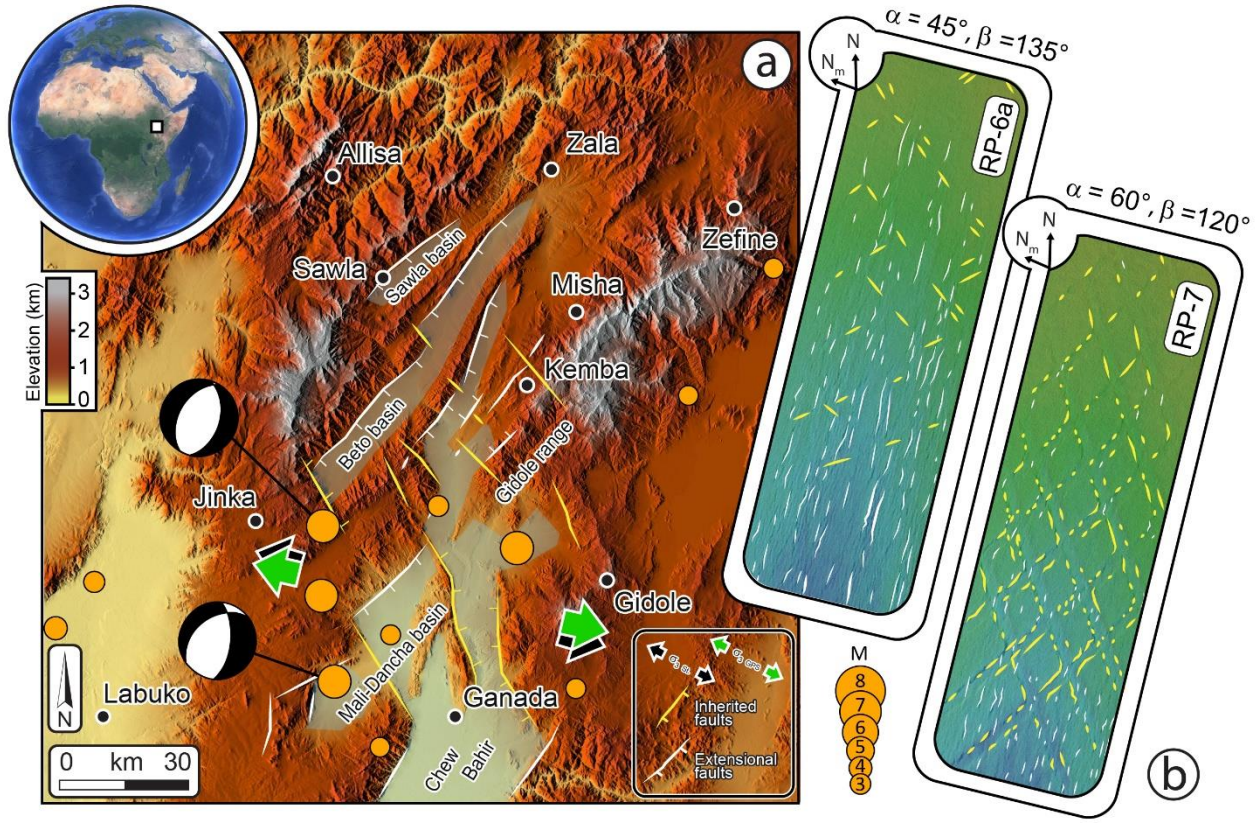

Figure 10. (a) Main structures of the Gofa Province (Ethiopia). Rift-related faults (white lines), are consistent with a north-eastward directed rift propagation, and are offset by inherited faults in the basement (yellow lines). Black arrows indicate σ_3 direction of extension as derived from structures, while green arrows indicate σ_3 direction as obtained from GPS. Orange dots show historical earthquakes (time interval 1900-2020). Seismicity and focal mechanisms for earthquakes with M≥3 are plotted from the USGS Earthquake Catalogue available at https://www.usgs.gov/natural-hazards/earthquake-hazards/earthquakes. **(b)** Models RP-6a and RP-7 (right panels) testing the role of inherited structures trending similar to those observed in the Gofa Province. Extension directions obtained from fault-slip data (black arrows; Philippon e al. (2014) and GPS vectors (green arrows; Kogan et al., (2012) are reported. Models RP-6a and RP-7 have been rotated to fit the natural setting.

4.2.3. Gulf of Suez

A third natural example is the Gulf of Suez, Egypt (Fig. 11a, b), which represents the ~350 km long northern continuation of the propagating, and partly oceanized, Red Sea. The evolution of the Red Sea-Gulf of Aden system is driven by triple-junction dynamics related to the African and Arabian plates. Bosworth et al. (2005) hypothesized a three-stage evolutionary model, the last of which implies rotation around an Eulerian pole that provided the basis of analogue modelling experiments addressing the Red Sea with a rotational tectonic setup (e.g., Molnar et al., 2017; 2018; 2020). The Gulf of Suez represents an interesting case for comparison, since inherited structures in the Precambian basement have been mapped and hypothesized to control the pattern of rift-related faults during north-westwards propagation of rifting. Inherited structures were identified by McClay & Khalil (1998) as ~N-trending faults, fractures and shear zones in the Esh El Mallha area and in the Hadaid block (EEM and HB in Fig. 11a), while

Younes & McClay (2002) documented the reactivation of the Ekma and Durba faults as transfer zones (Ekma-Durba Transfer Fault System, EDTFS in Fig. 11a). The reactivation of these structures (for the EDTFS also supported by the localization of historical seismicity; Fig. 11a) under an N60° directed extension (Younes & McClay; 2002) compares well with the setting of Model RP-3 (Fig. 11c), which tested S2 discontinuities with β=125°. The latter represents the average angle between the instantaneous stretching direction (ISD) and the inherited faults in the three areas of interest. Model RP-3 showed that such inherited structures fall in the experimental reactivation field (Fig. 7b) and thus could have been favourably oriented for reactivation. These structures often act as transfer zones (cf. areas marked by yellow dashed circles in Fig. 11c), which displace the pattern of rift-related faults, and show a good correlation between our models and this natural examples. A deviation from this favourable comparison is represented by the absence of the steep rift margins observed in the Gulf of Suez system, which are not reproduced in our models. This is likely due to the experimental setup architecture, which was designed to distribute deformation and avoid localization of deformation at the velocity discontinuity (VD). In this regard, a stronger influence of the VD may have improved this similarity.

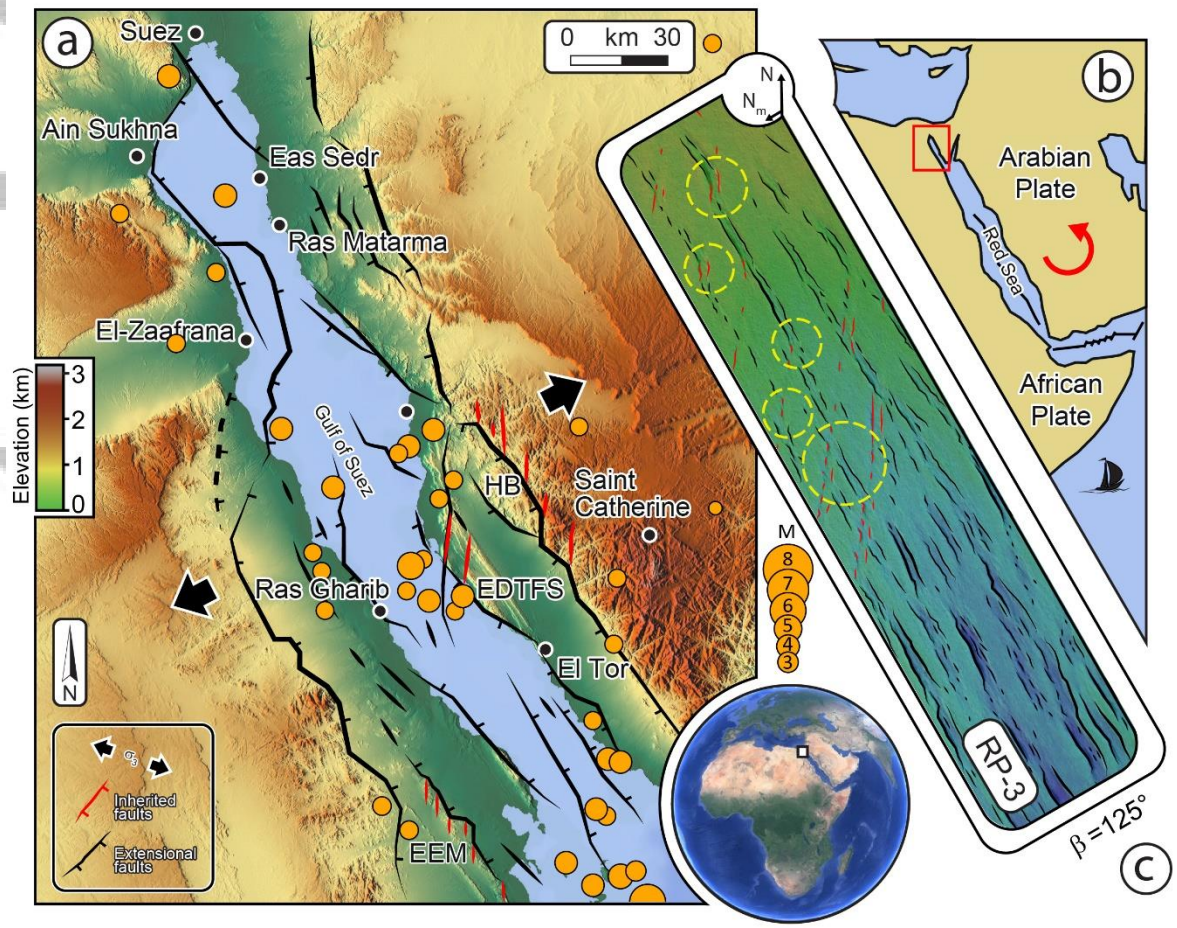

Figure 11. (a) The Gulf of Suez (Egypt), which is the **(b)** northern part of the Red Sea-Gulf of Aden rift system. Rift propagation is related to the final evolutionary stage of the system, implying the counter-clockwise rotation **(b)** of the Arabian Plate and the opening of the two rifts (Bosworth et al., 2005). Structures in **(a)** are mapped after Moustafa and El-Raey (1993) and Younes and McClay (2002), while orange dots show historical earthquakes (time interval 1900-2020). Seismicity and focal mechanisms are plotted for earthquakes with M≥3 from the USGS Earthquake Catalogue available at https://www.usgs.gov/natural-hazards/earthquake-hazards/earthquakes. **(c)** Model RP-3 showing the reactivation of inherited discontinuities as transfer zones (trending at 125° to the

direction of σ_3), and displacing the pattern of rift-related faults. Model RP-3 has been rotated to fit the natural setting.

4.2.4. Kenya Rift

The Kenya Rift (KR) is one of the major rifts segments of the East African Rift System (EARS) (e.g., Morley, 1999a) and it has propagated from the Turkana depression toward the Tanzania Divergence to the south (Fig. 12a,b; Nyblade & Brazier, 2002). Focal mechanisms in the northern sector show dip-slip to transtensional solutions aligned with the main rift-related structures. A similar pattern occurs in the southern sector, but with a higher complexity due to the interaction with the Tanzania Divergence. The southward propagation was likely induced by the clockwise rotation of the Somalian Block (e.g., Bonini et al., 2005; Fernandes et al., 2004; Nocquet et al., 2006) (Fig. 12c). The Kenya Rift also shows some curvature as a result of interaction with the Tanzanian Craton, whose rotation is also partly responsible for the northward propagation of the Tanganyka Rift. The areas surrounding the Kenya Rift have been shown to be largely shaped by the presence of inherited basement structures, with a wide range of orientations. Many of these structures are parallel to the major NW-SE-trending Aswa Shear Zone (Le Turdu et al., 1999; Morley, 1999b; Muirhead & Kattenhorn, 2017). Inherited faults associated with this major lineament interact with the Kenya Rift. For example, the Kordjya Fault System ($\alpha \approx 65°$) in the Magadi Basin is interpreted to result from the interaction between rift-related faults (white lines in Fig. 12c) and inherited faults (yellow lines in Fig. 12c) (Muirhead & Kattenhorn, 2017). Model RP-7 shows similarities with the Kenya Rift (Fig. 12d), as rift-related faults reactivated inherited fault segments with $\alpha \approx 60°$. The interaction between rift-related and inherited faults formed structural patterns that are similar to the Kordjya Fault system in the Magadi Basin (compare Fig. 12c and Fig.12e). Furthermore, seismicity localized on some of the inherited structures (Fig. 12a) records extensional to transtensional focal mechanisms, an indication that such structures may be reactivated under the current extensional stress field, in a similar fashion to our models.

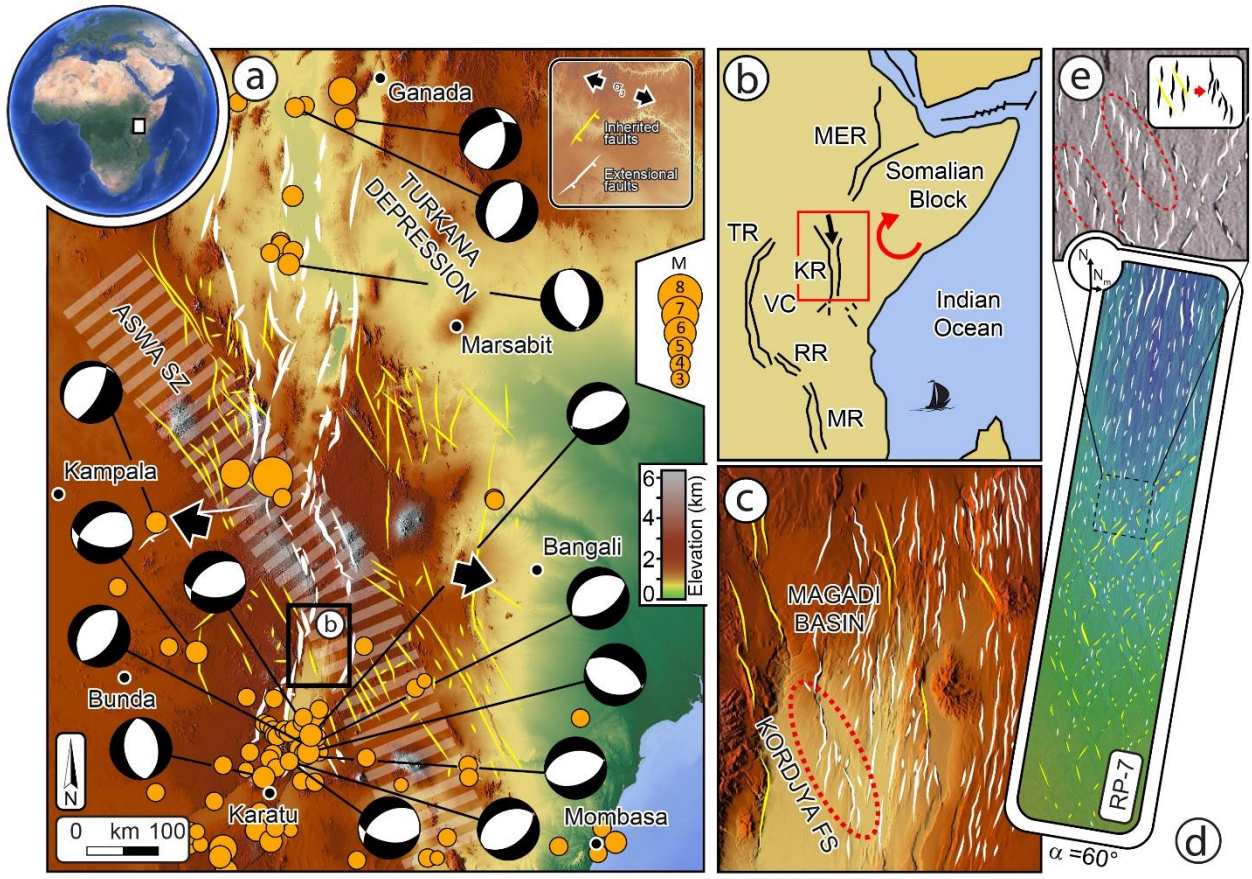

Figure 12. **(a)** The Kenya Rift is part of **(b)** the East African Rift System (EARS). The Kenya Rift shows extensional faults (white lines) propagating and interacting with inherited basement structures (yellow lines). The latter are often reactivated by rift propagation, as for **(c)** the Kordjya Fault System, in the Magadi Basin. MER: Main Ethiopian Rift; TR: Tanganyka Rift; KR: Kenya Rift; TC: Tanzanian Craton; RR: Rukwa Rift; MR: Malawi Rift. Structures in **(a)** are re-drown from Morley, 1999a; Morley et al., 1999; Vetel et al. (2005) and structures in **(c)** from Muirhead & Kattenhorn (2017). Trend of regional extension direction (σ_3) is from Muirhead & Kattenhorn (2017). Orange dots in **(a)** show historical earthquakes (time interval 1900-2020). Seismicity and focal mechanisms for earthquakes with M≥3 are plotted from the USGS Earthquake Catalogue available at https://www.usgs.gov/natural-hazards/earthquake-hazards/earthquakes. **(d)** Model RP-7 shows inherited faults (α=60°) with trend similar to those observed in the Magadi Basin ($\alpha\approx$65°). Model RP-7, particularly the area displayed in **(e)** show a fault reactivation pattern similar to the one observed in the Magadi basin and the Kordjya Fault System. Model RP-7 has been rotated to fit the natural setting.

5. Concluding remarks

We performed rotational extensional experiments in order to investigate the interaction between propagating rifts and pre-existing brittle crustal fabrics. The orientation of pre-existing discontinuities was varied relative to the extension direction. Our models provide general and specific insights into the rotational rift propagation process and the possible structural evolution of some specific natural systems. We summarize our main findings below:

- Our models reproduced rift propagation in terms of density of structures, number and depth of grabens, and the overall crustal thinning toward the pole of rotation. Models are comparable in general terms with existing processes described in the literature.
- The results of modelling provide new insights into the reactivation of inherited structures, suggesting that the reactivation field is delimited by angle ≥ 45° to the extension direction.

- Depending on their orientation, reactivated inherited faults often acted as transfer faults or oblique-slip faults. High-angle inherited faults, although not reactivated, may also act as accommodation zones. These features have the ability to offset rift propagation segments (i.e., exerting respectively hard and soft linkage effects) generating fault patterns similar to some natural examples.
- Gradients of reactivation were defined as a function of the distance from the pole of rotation and the trend of the inherited structure.
- Large-scale similarities are found between our models and the Trans-Mexican Volcanic Belt, as well as the local-scale setting of the Morelia Acambay Fault System and the Los Humeros and Acoculco areas. Here, inherited discontinuities were reactivated as transfer faults and may interact with rift-related faults.
- Our models also show similarities to other continental rifts, particularly the Gofa Province, the Gulf of Suez and Kenya Rift. In all these cases, inherited structures have strongly interacted with propagating rift segments, often acting as transfer zones.

Acknowledgments and Data

The research leading to these results has received funding from the GEMex Project, Europe-Mexico cooperation, under Horizon 2020 Research and Innovation Programme (grant agreement No. 727550). We kindly acknowledge the CFE (Comisión Federal de Electricidad) for supporting the GEMex project and for sharing data with the GEMex partners. We acknowledge Alexander R. Cruden, Daniele Trippanera and an anonymous Reviewer for the careful revision of the manuscript and the constructive comments that greatly improved the quality of our work. We are grateful to Federico Sani for the helpful discussion on the propagating rifts of the East African Rift system, which improved the comparison with the Kenya rift prototype. We also thank Frank Zwaan for his advices into rotational tectonics. All the data supporting this research are available in the text, in the Appendix, and in the in-text citation (Maestrelli et al, 2020) free to download at the following link http://doi.org/10.5281/zenodo.3724666 under Creative Commons Attribution 4.0 International Licence. We declare no conflict of interest.

References

Autin, J., Bellahsen, N., Leroy, S., Husson, L., Beslier, M. O., & d'Acremont, E. (2013). The role of structural inheritance in oblique rifting: Insights from analogue models and application to the Gulf of Aden. *Tectonophysics, 607*, 51-64. https://doi.org/10.1016/j.tecto.2013.05.041

Avellán, D. R., Macías, J. L., Layer, P. W., Cisneros, G., Sánchez-Núñez, J. M., Gómez-Vasconcelos, M. G., Pola, A., Sosa-Ceballos, G., García-Tenorio, F., Reyes Agustín, G., Osorio-Ocampo, S., García-Sánchez, L., Mendiola, I.F., Marti, J., López-Loera H., Benowitz, J. (2019). Geology of the late Pliocene–Pleistocene Acoculco caldera complex,

eastern Trans-Mexican Volcanic Belt (México). *Journal of Maps, 15(2)*, 8-18. https://doi.org/10.1080/17445647.2018.1531075

Avellán, D. R., Macías, J. L., Layer, P. W., Sosa-Ceballos, G., Gómez-Vasconcelos, M. G., Cisneros-Máximo, G., ... & Pola, A. (2020). Eruptive chronology of the Acoculco caldera complex–A resurgent caldera in the eastern Trans-Mexican Volcanic Belt (México). Journal of South American Earth Sciences, 98, 102412. https://doi.org/10.1016/j.jsames.2019.102412

Bellahsen, N., & Daniel, J. M. (2005). Fault reactivation control on normal fault growth: an experimental study. *Journal of Structural Geology, 27(4)*, 769-780. https://doi.org/10.1016/j.jsg.2004.12.003

Bellahsen, N., Fournier, M., d'Acremont, E., Leroy, S., & Daniel, J. M. (2006). Fault reactivation and rift localization: Northeastern Gulf of Aden margin. *Tectonics, 25(1)*. https://doi.org/10.1029/2004TC001626

Benes, V., & Scott, S. D. (1996). Oblique rifting in the Havre Trough and its propagation into the continental margin of New Zealand: comparison with analogue experiments. Marine Geophysical Researches, 18(2-4), 189-201. https://doi.org/10.1007/BF00286077

Bonini, M., Souriot, T., Boccaletti, M. & Brun, J.P. (1997). Successive orthogonal and oblique extension episodes in a rift zone: Laboratory experiments with application to the Ethiopian Rift, *Tectonics*, *16*, 347–362.

Bonini, M., Corti, G., Innocenti, F., Manetti, P., Mazzarini, F., Abebe, T., & Pecskay, Z. (2005). Evolution of the Main Ethiopian Rift in the frame of Afar and Kenya rifts Propagation. *Tectonics, 24(1)*. https://doi.org/10.1029/2004TC001680

Bosworth, W., P. Huchon, and K. McClay (2005), The Red Sea and Gulf of Aden basins, J. Afr. Earth Sci., 43(1–3), 334–378, doi:10.1016/j.jafrearsci.2005.07.020.

Brune, S., Corti, G., & Ranalli, G. (2017). Controls of inherited lithospheric heterogeneity on rift linkage: Numerical and analog models of interaction between the Kenyan and Ethiopian rifts across the Turkana depression. *Tectonics, 36(9)*, 1767-1786. https://doi.org/10.1002/2017TC004739

Buck, W. R. (1991). Modes of continental lithospheric extension. Journal of Geophysical Research: *Solid Earth, 96(B12)*, 20161-20178. https://doi.org/10.1029/91JB01485

Campos-Enriquez, J., & Garduño-Monroy, V. H. (1987). The shallow structure of Los Humeros and Las Derrumbadas geothermal fields, Mexico. *Geothermics, 16(5-6)*, 539-554. https://doi.org/10.1016/0375-6505(87)90038-1

Carrasco-Núñez, G., López-Martínez, M., Hernández, J., & Vargas, V. (2017). Subsurface stratigraphy and its correlation with the surficial geology at Los Humeros geothermal field, eastern Trans-Mexican Volcanic Belt. *Geothermics, 67,* 1-17. http://dx.doi.org/10.1016/j.geothermics.2017.01.001

Corti, G., Bonini, M., Conticelli, S., Innocenti, F., Manetti, P., & Sokoutis, D. (2003). Analogue modelling of continental extension: a review focused on the relations between the patterns of deformation and the presence of magma. *Earth-Science Reviews*, *63*(3-4), 169-247. https://doi.org/10.1016/j.jsg.2019.103946

Corti, G. (2009). Continental rift evolution: from rift initiation to incipient break-up in the Main Ethiopian Rift, East Africa. *Earth-Science Reviews, 96(1-2)*, 1-53. https://doi.org/10.1016/j.earscirev.2009.06.005

Corti, G., van Wijk, J., Cloetingh, S., & Morley, C. K. (2007). Tectonic inheritance and continental rift architecture: Numerical and analogue models of the East African Rift system. *Tectonics, 26(6)*. https://doi.org/10.1029/2006TC002086

Corti, G. (2012). Evolution and characteristics of continental rifting: Analog modeling-inspired view and comparison with examples from the East African Rift System. *Tectonophysics, 522*, 1-33. https://doi.org/10.1016/j.tecto.2011.06.010

Corti G., Molin P., Sembroni A., Bastow I.D., Keir D. (2018). Control of pre-rift lithospheric structure on the architecture and evolution of continental rifts: insights from the Main Ethiopian Rift, East Africa. *Tectonics, 37*, 477-496. https://doi.org/10.1002/2017TC004799

Del Ventisette, C., Bonini, M., Agostini, A., Corti, G., Maestrelli, D., & Montanari, D. (2019). Using different grain-size granular mixtures (quartz and K-feldspar sand) in analogue extensional models. *Journal of Structural Geology, 129*, 103888. https://doi.org/10.1016/j.jsg.2019.103888

Donnadieu, F., Kelfoun, K., de Vries, B. V. W., Cecchi, E., & Merle, O. (2003). Digital photogrammetry as a tool in analogue modelling: applications to volcano instability. *Journal of Volcanology and Geothermal Research, 123(1-2)*, 161-180. https://doi.org/10.1016/S0377-0273(03)00034-9

Fernandes, R. M. S., Ambrosius, B. A. C., Noomen, R., Bastos, L., Combrinck, L., Miranda, J. M., & Spakman, W. (2004). Angular velocities of Nubia and Somalia from continuous GPS data: implications on present-day relative kinematics. *Earth and Planetary Science Letters, 222(1)*, 197-208. https://doi.org/10.1016/j.epsl.2004.02.008

Ferrari, L. (2004). Slab detachment control on mafic volcanic pulse and mantle heterogeneity in central Mexico. *Geology, 32(1)*, 77-80. https://doi.org/10.1130/G19887.1

Ferrari, L., Orozco-Esquivel, T., Manea, V., & Manea, M. (2012). The dynamic history of the Trans-Mexican Volcanic Belt and the Mexico subduction zone. *Tectonophysics, 522*, 122-149. https://doi.org/10.1016/j.tecto.2011.09.018

Ferrill, D.A., Winterle, J., Wittmeyer, G., Sims, D., Colton, S., Armstrong, A. & Morris, A.P. (1999). Stressed rock strains groundwater at Yucca Mountain, Nevada. *GSA Today, 9(5)*, pp.1-8.

Garcıa-Palomo, A., Macıas, J. L., & Garduño, V. H. (2000). Miocene to recent structural evolution of the Nevado de Toluca volcano region, Central Mexico. Tectonophysics, 318(1-4), 281-302.

García-Palomo, A., Macías, J. L., Jiménez, A., Tolson, G., Mena, M., Sánchez-Núñez, J. M., ... & Lermo-Samaniego, J. (2018). NW-SE Pliocene-Quaternary extension in the Apan-Acoculco region, eastern Trans-Mexican Volcanic Belt. *Journal of Volcanology and Geothermal Research, 349*, 240-255. https://doi.org/10.1016/j.jvolgeores.2017.11.005

Garduño-Monroy, V. H., Pérez-Lopez, R., Israde-Alcantara, I., Rodríguez-Pascua, M. A., Szynkaruk, E., Hernández-Madrigal, V. M., ... & García-Estrada, G. (2009). Paleoseismology of the southwestern Morelia-Acambay fault system, central Mexico. *Geofísica internacional, 48(3)*, 319-335.

Gómez-Tuena, A., Orozco-Esquivel, M. T., & Ferrari, L. (2007). Igneous petrogenesis of the Trans-Mexican volcanic belt. *Geological Society of America Special Papers, 422*, 129-181.

Healy, D., Rizzo, R. E., Cornwell, D. G., Farrell, N. J., Watkins, H., Timms, N. E., ... & Smith, M. (2017). FracPaQ: A MATLAB™ toolbox for the quantification of fracture patterns. *Journal of Structural Geology, 95*, 1-16. https://doi.org/10.1016/j.jsg.2016.12.003

Gómez-Vasconcelos, M. G., Luis Macías, J., Avellán, D. R., Sosa-Ceballos, G., Garduño-Monroy, V. H., Cisneros-Máximo, G., ... & Perton, M. (2020). The control of preexisting faults on the distribution, morphology, and volume of monogenetic volcanism in the Michoacán-Guanajuato Volcanic Field. Geological Society of America Bulletin. https://doi.org/10.1130/B35397.1

Heidbach, O., Rajabi, M., Reiter, K., Ziegler, M. (2016): World Stress Map 2016, GFZ Data Service, doi:10.5880/WSM.2016.002.

Hubbert, M. K. (1937). Theory of scale models as applied to the study of geologic structures. *Bulletin of the Geological Society of America, 48(10)*, 1459-1520.

Kogan, L., Fisseha, S., Bendick, R., Reilinger, R., McClusky, S., King, R., & Solomon, T. (2012). Lithospheric strength and strain localization in continental extension from observations of the East African Rift. *Journal of Geophysical Research: Solid Earth, 117(B3)*. https://doi.org/10.1029/2011JB008516

Le Turdu, C., Tiercelin, J. J., Richert, J. P., Rolet, J., Xavier, J. P., Renaut, R. W., ... & Coussement, C. (1999). Influence of preexisting oblique discontinuities on the geometry and evolution of extensional fault patterns: evidence from the Kenya Rift using SPOT imagery. In *Geoscience of Rift Systems–Evolution of East Africa (Vol. 44, pp. 173-191)*. American Association of Petroleum Geologists Tulsa, OK, USA.

Liotta, D., and WP4 Working Group, (2019). Final report on active systems: Los Humeros and Acoculco. *Deliverable 4.1, GEMex project, European Union's Horizon 2020 programme, 334 pp*.

Maestrelli, Daniele, Montanari, Domenico, Corti, Giacomo, Del Ventisette, Chiara, Moratti, Giovanna, & Bonini, Marco. (2020). Analogue models testing the interaction between a propagating continental rift and inherited crustal fabrics *[Data set]. Zenodo.* http://doi.org/10.5281/zenodo.3724666

Mart, Y., & Dauteuil, O. (2000). Analogue experiments of propagation of oblique rifts. *Tectonophysics, 316(1-2)*, 121-132. https://doi.org/10.1016/S0040-1951(99)00231-0

Mauldon, M., Dunne, W. M., & Rohrbaugh Jr, M. B. (2001). Circular scanlines and circular windows: new tools for characterizing the geometry of fracture traces. *Journal of Structural Geology, 23(2-3)*, 247-258. https://doi.org/10.1016/S0191-8141(00)00094-8

McClay, K., & Khalil, S. (1998). Extensional hard linkages, eastern Gulf of Suez, Egypt. *Geology, 26(6)*, 563-566. https://doi.org/10.1130/0091-613(1998)026<0563:EHLEGO>2.3.CO;2

Merle, O. & Abidi, N. (1995). Approche expérimentale du functionnement des rampes émergentes. *Bulletin de la Société Géologique de France, 166*, 439-450. https://doi.org/10.2113/gssgfbull.166.5.439

Molnar, N. E., Cruden, A. R., & Betts, P. G. (2017). Interactions between propagating rotational rifts and linear rheological heterogeneities: Insights from three-dimensional laboratory experiments. *Tectonics, 36(3)*, 420-443. https://doi.org/10.1002/2016TC004447

Molnar, N. E., Cruden, A. R., & Betts, P. G. (2018). Unzipping continents and the birth of microcontinents. *Geology, 46(5)*, 451-454. https://doi.org/10.1130/G40021.1

Molnar, N. E., Cruden, A. R., & Betts, P. G. (2019). Interactions between propagating rifts and linear weaknesses in the lower crust. *Geosphere*. https://doi.org/10.1130/GES02119.1

Molnar, N., Cruden, A., & Betts, P. (2020). The role of inherited crustal and lithospheric architecture during the evolution of the Red Sea: Insights from three dimensional analogue experiments. Earth and Planetary Science Letters, 544, 116377. https://doi.org/10.1016/j.epsl.2020.116377

Montanari, D., Agostini, A., Bonini, M., Corti, G. & Ventisette, C. (2017). The use of empirical methods for testing granular materials in analogue modelling. *Materials, 10(6)*, 635. https://doi.org/10.3390/ma10060635

Moore Jr, J. M., & Davidson, A. (1978). Rift structure in southern Ethiopia. *Tectonophysics, 46(1-2)*, 159-173. https://doi.org/10.1016/0040-1951(78)90111-7

Morley, C. K. (1999a). AAPG Studies in Geology# 44, Chapter 10: Aspects of Transfer Zone Geometry and Evolution in East African Rifts.

Morley, C. K. (1999b). AAPG Studies in Geology# 44, Chapter 9: Influence of Preexisting Fabrics on Rift Structure.

Morley, C. K., & Ngenoh, D. K. (1999). AAPG Studies in Geology# 44, Chapter 1: Introduction to the East African Rift System.

Moustafa, A. R., & El-Raey, A. K. (1993). Structural characteristics of the Suez rift margins. *Geologische Rundschau, 82(1)*, 101-109. https://doi.org/10.1007/BF00563273

Muirhead, J. D., & Kattenhorn, S. A. (2018). Activation of preexisting transverse structures in an evolving magmatic rift in East Africa. *Journal of Structural Geology, 106*, 1-18. https://doi.org/10.1016/j.jsg.2017.11.004

Nocquet, J. M., Willis, P., & Garcia, S. (2006). Plate kinematics of Nubia–Somalia using a combined DORIS and GPS solution. *Journal of Geodesy, 80(8-11)*, 591-607. https://doi.org/10.1007/s00190-006-0078-0

Norini, G., Carrasco-Núñez, G., Corbo-Camargo, F., Lermo, J., Rojas, J. H., Castro, C., ... & Piccardi, L. (2019). The structural architecture of the Los Humeros volcanic complex and geothermal field. *Journal of Volcanology and Geothermal Research, 381*, 312-329. https://doi.org/10.1016/j.jvolgeores.2019.06.010

Nyblade, A. A., & Brazier, R. A. (2002). Precambrian lithospheric controls on the development of the East African rift system. *Geology, 30(8)*, 755-758.

Pfiffner, O.A. & Ramsay, J.G., 1982. Constraints on geological strain rates: Arguments from finite strain states of naturally deformed rocks. *Journal of Geophysical Research*, *87* (B1), 311-321.Philippon, M., Corti, G., Sani, F., Bonini, M., Balestrieri, M. L., Molin, P. & Cloetingh, S. (2014). Evolution, distribution, and characteristics of rifting in southern Ethiopia. *Tectonics, 33(4)*, 485-508. https://doi.org/10.1002/2013TC003430

Phillips, T. B., Jackson, C. A., Bell, R. E., Duffy, O. B., & Fossen, H. (2016). Reactivation of intrabasement structures during rifting: A case study from offshore southern Norway. *Journal of Structural Geology, 91*, 54-73. https://doi.org/10.1016/j.jsg.2016.08.008

Phillips, T. B., Fazlikhani, H., Gawthorpe, R. L., Fossen, H., Jackson, C. A. L., Bell, R. E., ... & Rotevatn, A. (2019). The Influence of Structural Inheritance and Multiphase Extension

on Rift Development, the NorthernNorth Sea. *Tectonics*. https://doi.org/10.1029/2019TC005756

Pongwapee, S., Morley, C. K., & Won-in, K. (2019). Impact of pre-existing fabrics and multi-phase oblique extension on Cenozoic fault patterns, Wichianburi sub-basin of the Phetchabun rift, Thailand. *Journal of Structural Geology, 118*, 340-361. https://doi.org/10.1016/j.jsg.2018.11.012

Ramberg, H. (1981). Gravity, deformation and the earth's crust: in theory, experiments and geological application. Academic press.

Rotevatn, A., Kristensen, T. B., Ksienzyk, A. K., Wemmer, K., Henstra, G. A., Midtkandal, I., S.-A. Grundvåg & Andresen, A. (2018). Structural inheritance and rapid rift-length establishment in a multiphase rift: the East Greenland rift system and its Caledonian orogenic Ancestry. *Tectonics, 37(6)*, 1858-1875. https://doi.org/10.1029/2018TC005018

Schiffer, C., Doré, A. G., Foulger, G. R., Franke, D., Geoffroy, L., Gernigon, L., ... & Peace, A. (2019). Structural inheritance in the North Atlantic. *Earth-Science Reviews, 102975*. https://doi.org/10.1016/j.earscirev.2019.102975

Souriot, T., & Brun, J. P. (1992). Faulting and block rotation in the Afar triangle, East Africa: The Danakil" crank-arm" model. *Geology, 20(10)*, 911-914. https://doi.org/10.1130/0091-7613(1992)020<0911:FABRIT>2.3.CO;2

Thielicke, W and Stamhuis, E J 2014 PIVlab – Towards User-friendly, Affordable and Accurate Digital Particle Image Velocimetry in MATLAB. *Journal of Open Research Software, 2: e30*, DOI: http://dx.doi.org/10.5334/jors.bl

Vétel, W., Le Gall, B., & Walsh, J. J. (2005). Geometry and growth of an inner rift fault pattern: the Kino Sogo Fault Belt, Turkana Rift (North Kenya). *Journal of Structural Geology, 27(12)*, 2204-2222. https://doi.org/10.1016/j.jsg.2005.07.003

Weijermars, R. (1997). Principles of rock mechanics. Alboran Science Publishing.

Weijermars, R., Schmeling, H. (1986). Scaling of Newtonian and non-Newtonian fluid dynamics without inertia for quantitative modelling of rock flow due to gravity (including the concept of rheological similarity). *Physics of the Earth and Planetary Interiors 43*, 316–330. https://doi.org/10.1016/0031-9201(86)90021-X

Younes, A. I., & McClay, K. (2002). Development of accommodation zones in the Gulf of Suez-Red Sea rift, Egypt. *AAPG bulletin, 86(6)*, 1003-1026. https://doi.org/10.1306/61EEDC10-173E-11D7-8645000102C1865D

Zwaan, F., & Schreurs, G. (2017). How oblique extension and structural inheritance influence rift segment interaction: Insights from 4D analog models. *Interpretation, 5(1)*, SD119-SD138. https://doi.org/10.1190/INT-2016-0063.1

Zwaan, F., & Schreurs, G. (2020). Rift segment interaction in orthogonal and rotational extension experiments: Implications for the large-scale development of rift systems. Journal of structural geology, 140, 104119. https://doi.org/10.1016/j.jsg.2020.104119

Zwaan, F., Schreurs, G., & Rosenau, M. (2020). Rift propagation in rotational versus orthogonal extension: Insights from 4D analogue models. *Journal of Structural Geology, 103946*. https://doi.org/10.1016/j.jsg.2019.103946

Appendix A: Model scaling and analogue material characterization

Models were scaled to achieve a correct geometric, dynamic, rheological and kinematic similarity (Hubbert, 1937; Ramberg, 1981) (Table 1). Specifically, length and thickness (geometrical similarity) of models were scaled using a scaling ratio (defined as $l^*=l_{model}/l_{nature}$ and $h^*=h_{model}/h_{nature}$) of $6.67x10^{-6}$, such that 1 cm in the model corresponds to 15 km in nature. The modelling procedure was developed in normal gravity, so that the gravity scaling ratio (g^*) between the model and nature was equal to 1. The density of mixture of granular material (Quartz and K-feldspar) and silicone and Corundum (1440 kg m^{-3}) implied a density scaling ratio (ρ^*) of 0.53, considering a natural rock density of ~2700 kg m^{-3} leading to a stress scaling ratio ($\sigma^*=\rho^* g^* l^*$) of $3.53x10^{-7}$. The coefficient of internal friction (μ) requires to be similar both in the analogue material and the natural rock, implying a $\mu^* \sim 1$. In order to obtain dynamic scaling of models, cohesion ratio (c^*) needs to equal the stress ratio ($\sigma^*=c^*$), a condition that is fulfilled as c^* and σ^* share the same order of magnitude (10^{-7}) (Table 1).

Scaling of the ductile layer simulating the LC, implies the consideration of both viscosity and the strain rate. The LC was simulated with a mixture of PDMS and corundum sand. Corundum was added to PDMS in a quantity necessary to reach the correct density value of 1440 kg m^{-3}. In order to obtain a proper density of the PDMS-corundum mixture comparable to the density of the model UC (1440 kg m^{-3}), we empirically estimated a proportion of PDMS-Corundum of ~1:1 in weight. Viscosity of this material was measured using a coni-cylinder viscometer apparatus.

The viscosity of the model ductile lower crustal layer is relatively high, leading to a rather low brittle/ductile strength ratio. This will influence at some extent both the spacing of faults, which is expected to result in a larger number of faults and a wider region of deformation, and surface topography relief, which will be somewhat less amplified.

Through progressive steps, we calculated the shear-stress vs. strain rate curve for the PDMS-corundum material (Fig. A1). We obtained the following equation using regression line ($R^2=0.99$):

$$Y=2x10^{-6} X^{1.24}$$

where $Y=\dot{\varepsilon}$ ($\dot{\varepsilon}$ being the strain rate) and $X=\tau$ (τ being the shear stress):

$$\dot{\varepsilon} =2x10^{-6} \tau^{1.24}$$

In our case n = 1.24, and thus we have assumed the PDMS+corundum mixture as a near-Newtonian material. Viscosity is therefore extrapolated at model strain rate ($\dot{\varepsilon}_{mod}$) according to the following equations:

$$\eta= \tau / \dot{\varepsilon}_{mod}$$

$$\dot{\varepsilon}_{mod} =2x10^{-6} \tau^{1.24}$$

$\dot{\varepsilon}_{mod}$ was calculated from our models as the maximum $\dot{\varepsilon}_{mod}$ considering the linear deformation and the velocity at the proximal, left hand side of our model setup (see Fig. 2).

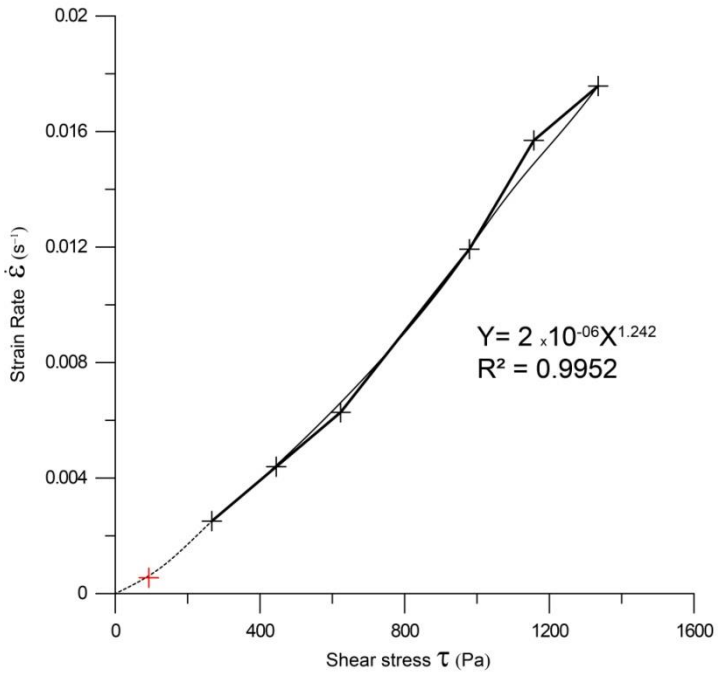

Figure A1. Graph showing the strain rate vs. shear stress curve for the used PDMS+corundum mixture obtained using the coni-cylinder viscometer, from which was extrapolated the viscosity value (red cross) at experimental strain rates.

The maximum engineering strain rate, $\dot{\varepsilon}_{mod}$, has been calculated as follow:

$$\dot{\varepsilon}_{mod} = d/(t*h)$$

where d is the final length between the corners of the moving plates (d=0.08 m), t is the cumulative time of deformation (t=14400 s) and h the thickness of the viscous layer (h=0.01 m). From this follows:

$$\dot{\varepsilon}_{mod} = 0.08/(14400 \times 0.01) = 5.55 \times 10^{-4}\ s^{-1}$$

We can now extrapolate τ from the following equation:

$$\dot{\varepsilon}_{mod} = 2 \times 10^{-6}\ \tau^{1.24}$$

$$5.55 \times 10^{-4} = 2 \times 10^{-6}\ \tau^{1.24}$$

$$\tau = 92.73\ Pa$$

We have therefore obtained a value of effective viscosity η_m for the model of:

$$\eta_m = \tau / \dot{\varepsilon}_{mod} = 92.73/5.55 \times 10^{-4} = 1.69 \times 10^5\ Pa\ s$$

Assuming prototype viscosity values η_n of the lower continental crust in the range 10^{20} and 10^{24} Pa s (e.g. Weijermars, 1997), and considering model viscosity $\eta_m = 1.69 \times 10^5$ Pa s, the viscosity ratio η* ranges from 1.69×10^{-15} up to 1.69×10^{-19}. One can thus obtain $\dot{\varepsilon}^*$ from $\dot{\varepsilon}^* = \sigma^*/\eta^*$, such that ε* ranges from 2.1×10^8 to 2.1×10^{12}. For an average viscosity of 10^{22} Pa s, we obtain $\varepsilon^* = 2.1 \times 10^{10}$, which corresponds to a natural strain rate of 2.66×10^{-14} s^{-1}. The latter value falls within the range of natural strain rates, which broadly varies from 10^{-13} s^{-1} to 10^{-15} s^{-1} (Pfiffner & Ramsay, 1982). Following Merle & Abidi (1995), the horizontal displacement rate $v^* = v_m/v_n$ is given by the product of ε* and l^*, such that an average viscosity of 10^{22} Pa s (for which $\varepsilon^* = 2.1 \times 10^{10}$) corresponds to a natural extension rate of $v_n = v_m/v^* = 5.55 \times 10^{-6}/1.4 \times 10^4 \approx 12.5$ mm yr^{-1} (Table 1).

Dynamic similarity of the viscous layer can be effectively defined by the dimensionless ratio R_m of gravitational to viscous forces (Ramberg, 1981), termed 'Ramberg number' (R_m) by Weijermars & Schmeling (1986):

$$R_m = \frac{F_g}{F_v} = \frac{\rho_d g z_d}{\eta \dot{\varepsilon}} = \frac{\rho_d g z_d^2}{\eta v},$$

where ρ_d and z_d are the density and thickness of the ductile layer, g is the gravitational acceleration, η is the viscosity, $\dot{\varepsilon}$ is the strain rate given by the ratio between the velocity v and the thickness of the ductile layer. In nature, R_m can be estimated to be about 1.6 (considering ρ_n = 2900 kg m^3, g = 9.81 m s^{-2}, h = 15 km, $\eta_n = 10^{22}$ Pa s, and v_n=12.5 mm yr^{-1}), while in the model R_m can be estimated at 1.5 (considering ρ_m = 1440 kg m^3, g = 9.81 m s^{-2}, h = 0.01 m, $\eta_m = 1.69 \times 10^5$ Pa s, and v_m=20 mm hr^{-1}; Table 1).

Dynamic similarity of the brittle layer can be estimated using the ratio S_m of gravitational to frictional forces in model and nature (Corti et al., 2003), which is essentially equivalent to the Smoluchowsky number (S_m) defined by Ramberg (1981):

$$S_m = \frac{F_g}{F_f} = \frac{\rho_b g z_b}{\mu \rho_b g z_b + c_0},$$

where ρ_b and z_b are the density and thickness of the brittle layer, g is the gravitational acceleration, c is the cohesion, and μ is the internal friction coefficient. In nature, S_m can be estimated to be about 1.6 (considering ρ_n = 2700 kg m^3, g = 9.81 m s^{-2}, μ = 0.6, h = 15 km, and $c_o \approx 10^7$ Pa), while in the model S_m can be estimated at ~1.5 (considering ρ_n = 1440 kg m^3, g = 9.81 m s^{-2}, μ = 0.6, h = 0.01 m, and $c_o \approx 6$ Pa). Since both nature and models share very similar R_m and S_m numbers, the requirement of dynamic similarity is fulfilled.

The Reynolds number, R is another dimensionless number (ratio of inertial to viscous forces) relevant for the modelling, which is given as (Ramberg, 1981, notations as above):

$$R_e = \frac{F_i}{F_v} = \frac{\rho v z_d}{\eta}.$$

However, R_e numbers cannot be equivalent in model and nature, even though a dynamic similarity with natural conditions can be obtained for analogue models deformed under a natural gravitational field whether $R_e << 1$ and inertial forces can be considered as negligible, which leads to the 'quasi-static' approximation (Hubbert, 1937; Ramberg, 1981). More specifically, the lack of a strict equivalence of Reynolds numbers in model and nature can be disregarded when inertias are negligible, that is when (Ramberg, 1981) "acceleration, in terms of rate of change of velocity, but certainly not in terms of force per unit mass in a body-force field, of most tectonic processes is negligible except, for example, in earthquakes". R_e estimated for our models yields a value of 4.7 x 10^{-10}, which is small enough to fulfil the quasi-static' approximation.

Appendix B: PIV analysis example on model RP-1

PIV analysis was performed on specific models to highlight the gradient of deformation. The latter decreases toward the pole of rotation, with the velocities being zero along the central axis of the experiment (Fig. A2a, b). The graph in Figure A2c indicates a rift-axis parallel decrease in deformation velocity along profiles A-A' and B-B'. In early stages of deformation, the vectors highlight the presence of a boundary effect in the distal side of the area of interest, which is due to rubber sheet compression along the direction of rift propagation. The presence of this boundary effect suggested us to restrict the area of analysis, excluding the distal part of the model. Overall, the velocity gradient highlighted by PIV analysis reflects well the gradient of deformation propagating toward the rotation pole.

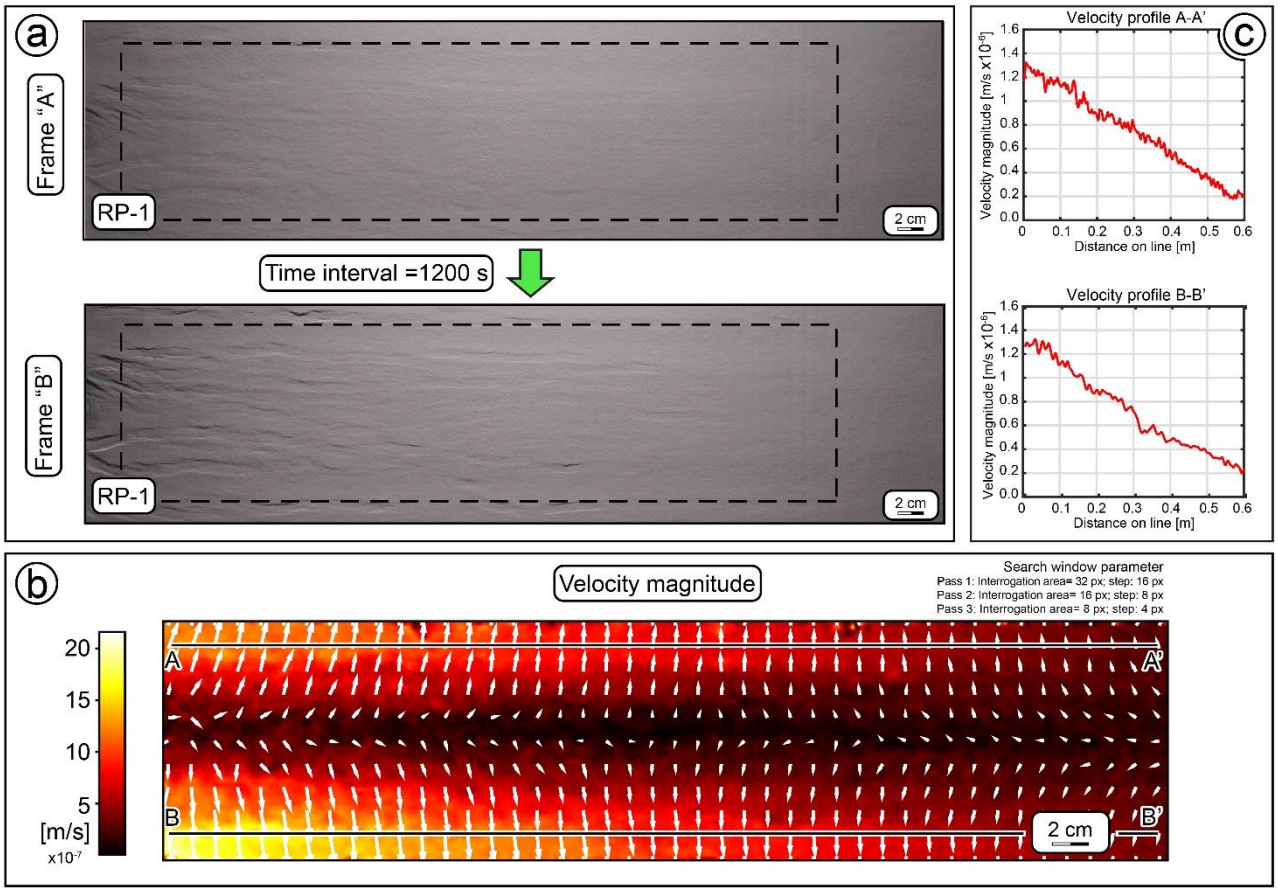

Figure A2. **(a)** Frames "A" and "B" used to calculate displacement vectors by applying PIV analysis to model RP-1 (time interval between the two frames is 1200 seconds). Search window parameters are reported in **(b)**, which shows the result of the analysis. Background colours indicate velocity magnitude. **(c)** Graphs showing the velocity gradient sampled along profiles A-A' and B-B' (shown in **b**), with velocity progressively decreases toward the rotation pole.

Appendix C: Dilation Tendency of inherited structures of the Trans-Mexican Volcanic Belt

Fault reactivation can be also analysed in terms of Dilation Tendency. Figure S2 shows the Normalized Dilation Tendency (T_D, defined as the ratio $(\sigma_1-\sigma_n)/(\sigma_1-\sigma_3)$; Ferril et al., 1999) tested on the faults of Model RP-4, by applying a standard stress field compatible with crustal stretching imposed by model deformation (Fig. A3b, c). As expected, the most dilatant structures (T_D=1) are the W-E trending normal faults which developed as a direct effect of the imposed stress field. Nonetheless, T_D analysis shows that also reactivated discontinuities of set S2 may experience some dilation (with values sometimes being >8), especially in the area of linkage with rift-related faults (marked by warm colours on Fig. A3d). Even if we cannot consider the Dilation Tendency of a structure as a direct proxy for permeability, the propensity of a structure to be opened can represent a favourable condition for channelling upward magmatic fluids, which may in turn localize eruptive centres. This observation is in agreement with the hypothesis that Los Humeros and Acoculco calderas are bounded by inherited, rectilinear structures (e.g., Carrasco-Núñez et al., 2017) that might have favoured magma emplacement. This analysis therefore confirms that rift propagation may control both the large-scale and local-scale deformation patterns along the Trans-Mexican Volcanic Belt.

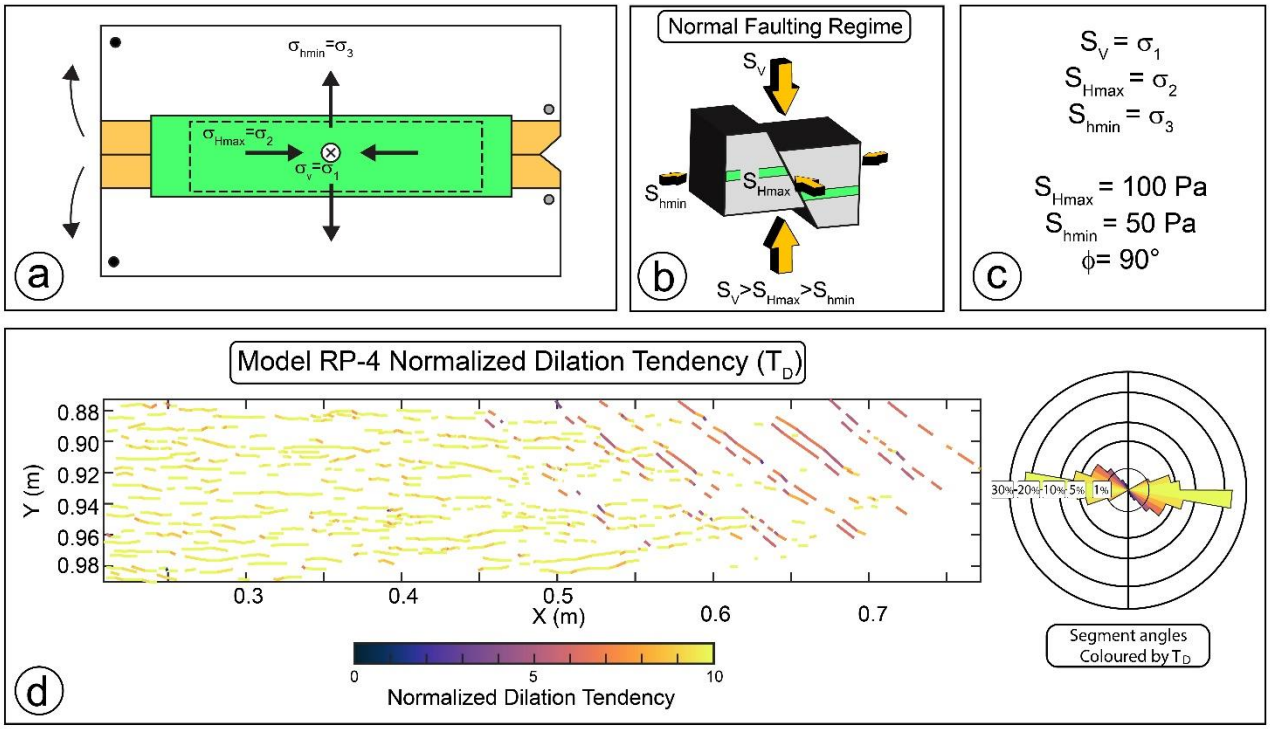

Figure A3. Normalized Dilation Tendency (T_D) applied to Model RP-4 using FracPaQ software. **(a)** Schematic sketch of the stress field acting on model. **(b)** Theoretical stress filed inducing a normal faulting regime. **(c)** Standard stress conditions assumed for the analysis of Dilation Tendency. Knowing the value of two principal stresses and the orientation of one of them (ϕ), it is possible to compute the 2D equivalent of the Dilation Tendency on fracture planes (Healy & Rizzo, 2017). Standard stresses in nature have been scaled to the model (at the base of the UC) using the stress scaling ratio. **(d)** Normalized T_D for Model RP-4. Reactivated structures show a normalized tendency to dilation, especially at the intersection with extension-related structures. The rose diagram shows fault segment orientation, coloured by T_D.